Ore Geology Reviews 157 (2023) 105422

Contents lists available at ScienceDirect

Ore Geology Reviews

journal homepage: www.elsevier.com/locate/oregeorev

REE ultra-rich karst bauxite deposits in the Pedernales Peninsula, Dominican Republic: Mineralogy of REE phosphates and carbonates

Cristina Villanova-de-Benavent [a,*], Joaquín A. Proenza [a], Lisard Torró [b], Thomas Aiglsperger [c], Cristina Domènech [a], Diego Domínguez-Carretero [a], Xavier Llovet [d], Pol Suñer [a], Australia Ramírez [e], Jesús Rodríguez [e]

[a] Departament de Mineralogia, Petrologia i Geologia Aplicada, Facultat de Ciències de la Terra, Universitat de Barcelona (UB), Martí i Franquès s/n, 08028 Barcelona, Spain
[b] Geological Engineering Program, Faculty of Sciences and Engineering, Pontifical Catholic University of Peru, Lima, Peru
[c] Dept. Civil Engineering and Natural Resources, Division of Geosciences and Environmental Engineering, Luleå University of Technology, Luleå, Sweden
[d] Centres Científics i Tecnològics, Universitat de Barcelona, Lluís Solé i Sabarís, 1-3, 08028 Barcelona, Spain
[e] Servicio Geológico Nacional, Av. Winston Churchill 75, Edificio "J. F. Martínez", Santo Domingo, Dominican Republic

ARTICLE INFO

Keywords:
Rare earth elements (REE)
Supergene deposits
Monazite
Secondary REE phosphates
Bastnäsite

ABSTRACT

Karst bauxites have recently received renewed attention for their potential as non-conventional REE sources. Karst bauxites from the Pedernales Peninsula in the Dominican Republic stand among the world's richest in REE. Bauxite ore from two deposits from this bauxite district, Aceitillar and El Turco, have been selected for this study due to their outstanding REE contents and contrasting mineralogy. REE (La to Lu) contents in Aceitillar, range from 0.07 to 0.16 wt%, and Y from 0.01 to 0.13 wt%, whereas El Turco contains between 0.28 and 1.40 wt% REE, and 0.33 to 1.48 wt% Y. The characterisation of REE mineralisation was performed through powder and monocrystal XRD, SEM-EDS, and EMP analyses. REE phosphates and carbonates reveal textural features that suggest significant REE mobilisation and re-deposition within the bauxite profile. The identified REE minerals can be classified into: i) primary monazite(-Ce) and minor monazite(-La); ii) secondary Y- and Nd-dominant phosphates; and iii) secondary Gd- and Nd-carbonates of the (hydroxyl)bastnäsite group. While monazites are ubiquitous in the two studied deposits, secondary phosphates are predominant in El Turco while secondary carbonates are exclusive of Aceitillar. This contrasting mineralogy is explained by the total concentration of carbonate and/or phosphate in the karst bauxite groundwater solutions. REE phosphates are the most stable phases at $[CO_3^{2-}]_{total}/[PO_4^{3-}]_{total} \leq 2$; whereas REE carbonates are stable at near neutral pH when the total aqueous carbonate concentration is two orders of magnitude higher than that of phosphate. Results of this investigation contribute to a better understanding of the formation REE minerals in the supergene environment and can be applied in REE separation methods.

1. Introduction

Bauxite ore is the main source for Al in the world (Bray, 2017). Karst bauxites—characterised by a strong association with a carbonate host (Bárdossy 1982) and representing 14 % of the bauxite resources worldwide (Mameli et al., 2007)—have gained interest recently also because of their capacity to accumulate rare earth elements (REE) (e.g., Mouchos et al., 2016; Deady et al., 2014; Mondillo et al., 2019; Yang et al., 2019). REE may be extracted as by-products in large-scale Al mines (Weng et al., 2015; Goodenough et al. 2017; Vind et al., 2018). REE are considered critical raw materials because of the increasing demand due to their numerous technological applications (e.g., power generation, advanced electronics, production of high-tech ceramics and glass), with individual REE often having no substitutes in specific applications (Wall, 2014; Smith Stegen, 2015). An additional factor contributing to their status as "critical" is that, around 60% of the current REE mine production is supplied by one country (China) (Cordier, 2021), and it has been over 80% for a long time (Chakhmouradian and Wall, 2012; Dutta et al., 2016; Gamboji, 2017; Goodenough et al., 2017; European Commission, 2020). Separation and refining operations are

* Corresponding author.
E-mail address: cvillanovadb@ub.edu (C. Villanova-de-Benavent).

https://doi.org/10.1016/j.oregeorev.2023.105422
Received 30 October 2022; Received in revised form 23 February 2023; Accepted 28 March 2023
Available online 31 March 2023

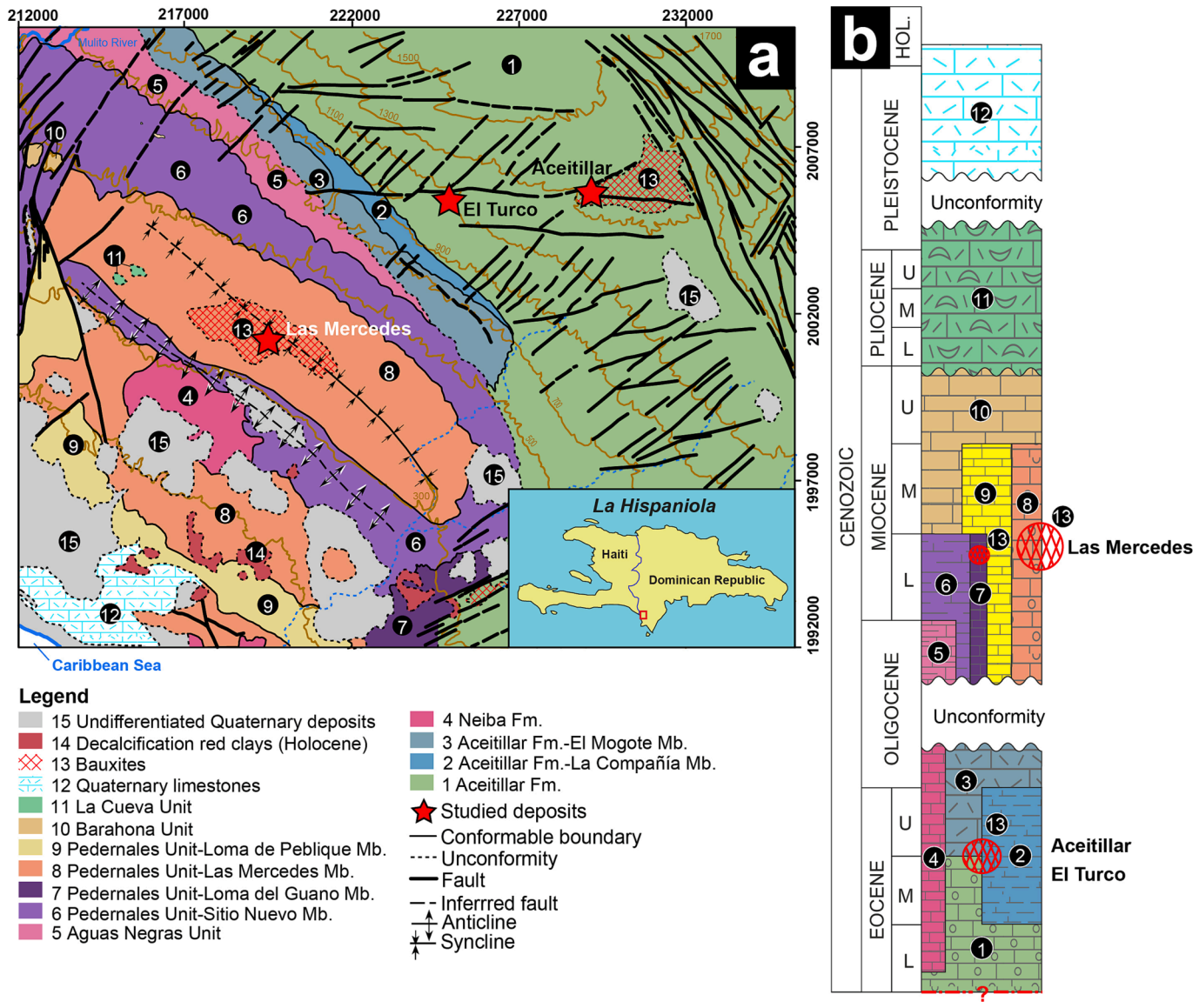

Fig. 1. Geological map of the study area in Sierra de Bahoruco, Pedernales Peninsula, including the deposits of Las Mercedes, El Turco, and Aceitillar, indicated by red stars. Map (a) modified from Pérez-Valera et al. (2010) and schematic lithostratigraphic column (b) modified from Torró et al. (2017). Key: Fm. = Formation; Mb. = Member.

also concentrated in a single country (China, with more than 90% of the market share in 2019) (International Energy Agency-IEA, 2021).

The karst bauxites of the Pedernales Peninsula (SW Dominican Republic) contain significant REE resources (Aiglsperger et al., 2019; Proenza et al., 2017; Torró et al., 2017; Villanova-de-Benavent et al., 2017, 2021, 2022; Ramírez, 2015). All the deposits of the district yield high total REE (La-Lu) contents, ranging from ~500 to ~14,000 ppm (~1,900 ppm on average), and from ~50 to ~15,000 ppm Y (~1,200 ppm on average). Two deposits of the Bahoruco district, Aceitillar and El Turco, stand out with average total REE contents of ~1,200 and ~7,600 ppm, and average Y contents of ~700 and ~8,800 ppm: Aceitillar and El Turco, respectively (Villanova-de-Benavent et al., 2017; Aiglsperger et al., 2019; Proenza et al., 2021). This study presents a first detailed characterisation of the REE-bearing minerals of these two karst bauxite deposits and discusses the processes that lead to the deposition of secondary REE phases. Our results provide evidence of authigenic REE-phosphate and REE-carbonate growth during bauxitisation and shed light on the conditions of formation of phosphates versus carbonates in weathering environments.

2. Geological setting

The studied karst bauxites are located in the Sierra de Bahoruco in the Pedernales Peninsula, SW Dominican Republic (Fig. 1). This Peninsula represents the eastern end of the Presqu'île Du Sud (Southern Peninsula) morphotectonic zone defined by Lewis and Draper (1991), and is limited to the north by the regional, W-E trending Plantain Garden-Enriquillo fault zone. Normal faults associated to the NNE-SSE trending Beata Ridge delineate its eastern limit. According to Pérez-Valera (2010), uplift and deformation in the Bahoruco Peninsula commenced in the Pliocene in response to the oblique convergence of the North American plate continental margin and the Caribbean island arc (see also Mann, 2007). Transpressive stresses are accommodated by a series of high-angle reverse and strike-slip faults and soft, km-scale folds geomorphologically resulting in extremely rugged relieves and ample development of karsts in the exposed carbonate strata.

The crystalline basement in the Bahoruco Peninsula is composed of Campanian to lower Eocene volcanic rocks of the Dumisseau Formation, an on-land portion of the Caribbean Large Igneous Province (CLIP; Lidiak and Anderson, 2015; Escuder-Viruete et al., 2016). This basement

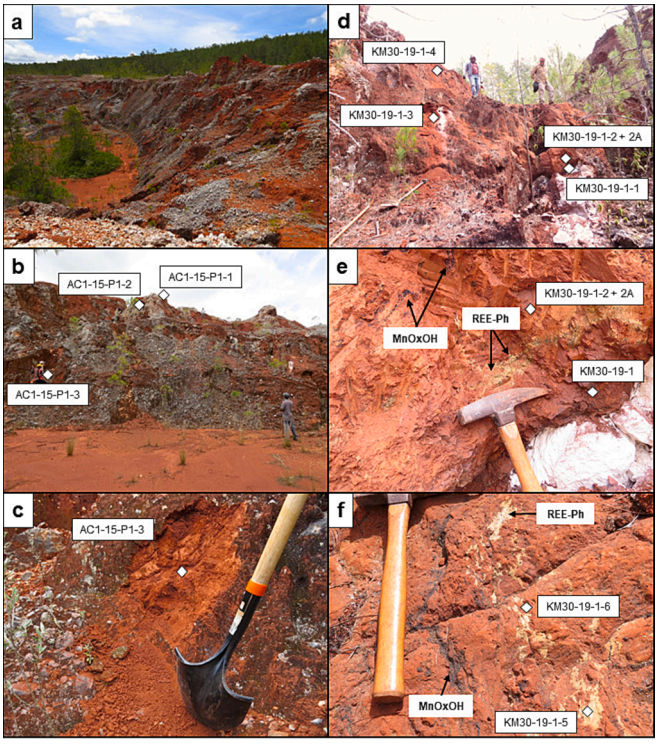

Fig. 2. Images of the old mining pits of Aceitillar (a-c) and El Turco (d-f). Note the yellow and black mineralisations in e) and f), which correspond to REE phosphates (REE-Ph) and Mn oxyhydroxides (MnOxOH), respectively. Specific sample sites are indicated by white diamonds with their associated sample number.

is overlain by a thick sequence of Eocene to Quaternary carbonate rocks, which include, bottom to top: 1) the Aceitillar and Neiba Formations of lower Eocene-Oligocene ages; 2) Aguas Negras, Pedernales, and Barahona units, of Upper Oligocene-Miocene ages; 3) La Cueva unit, of Pliocene-lower Pleistocene age; and 4) Pleistocene and Holocene carbonates linked to lagoon and pocket beaches (Fig. 1). The carbonate strata record a progressive shift in the environment of deposition from deep, outer slope during the Eocene through shallow, through inner platform and reef boundstones in the Pliocene, to emersion in the Pleistocene (de León, 1989; Pérez-Valera, 2010; Pérez-Valera and Abad, 2010). Materials associated with chemical weathering, including decalcification red clays and bauxite argillisations, are prevalent in the area and have developed since the Pleistocene (Pérez-Valera, 2010). They occur mostly in karst landforms on carbonate strata.

2.1. Geology of the bauxite deposits

The bauxite deposits in Sierra de Bahoruco have been mined discontinuously since 1959 and until 2016 by Alcoa Exploration Company and DOVEMCO S.A. (Domínico-Venezolana de Minería y Construcción; Dominican-Venezuelan Mining and Construction Company). The deposits are mainly hosted within Eocene-Oligocene (Aceitillar and Neiba Formations) and Miocene (Las Mercedes Member in the Pedernales Unit) carbonates. For a detailed description of the lithofacies in the three formations, the reader is referred to Pérez-Valera (2010), Pérez-Valera and Abad (2010), and Torró et al. (2017). The bauxite deposits fill karst cavities, are bag-shaped, and may reach thicknesses of 15 m (Fig. 2). Bauxites have a massive texture, an intense red colour, and are often overlain by up to 2-m-thick bauxitic clays (a.k.a. *terra rossa*).

The largest deposit is Las Mercedes, which was under exploitation until 2016 by DOVEMCO. The Las Mercedes deposit is located at an altitude below 450 m.a.s.l. (Fig. 1), where bauxites fill up a karst depression of 2.3 km^2 along the core of a SE-trending gentle syncline. Bauxite displays thicknesses between 8 and 10 m and is disrupted by carbonate pillars over a gentle hummock-shaped to flat base. Bauxite ore is massive and mostly composed of gibbsite with lesser amounts of kaolinite, hematite, boehmite, anatase, and goethite. Further detail on the geology, geochemistry, and mineralogy (including REE-bearing phases) of the Las Mercedes deposit can be found in Torró et al. (2017).

Most of the documented bauxite deposits in the district are located higher up relative to Las Mercedes, mostly between 1100 and 1900 m.a.s.l., and hosted in the Eocene-Oligocene carbonates (e.g., Aceitillar, El Turco, and Sombrero deposits; Fig. 1). In this area, bauxites are reddish-brown fine-grained material with small hard concretions (Goldich and Bergquist, 1947), and display thicknesses of a few metres to tens of metres (Fig. 2a), and may contain sterile limestone intercalations (Fig. 2b). The contact with the underlying limestone is sharp, but irregular-shaped (Goldich and Bergquist, 1947). Locally, these bauxites show black coloured zones, rich in Mn oxyhydroxides (Fig. 2c). The mineralogy of two of these deposits, Aceitillar and El Turco, is detailed below.

3. Materials and methods

For this study, two karst bauxite deposits from the Sierra de Bahoruco, El Turco and Aceitillar, were selected because of their distinctively high REE contents. Nine representative samples were collected in each deposit during two field work campaigns (Fig. 2). The samples consist of friable and/or loose, reddish brown material (Fig. 2a-d). In El Turco, this bauxitic material is locally cut by REE phosphate veinlets of yellow color (Fig. 2e-f).

Major, minor, and trace elements of bulk samples were determined at Activation Laboratories Ltd. (*Actlabs*, Ontario, Canada) by utilising the analytical package "4-Litho", which uses fusion inductively coupled plasma emission (FUS-ICP) and inductively coupled plasma emission mass spectrometry (ICP-MS; for details see *Lithogeochemistry* at https://www.actlabs.com).

The general mineralogy of the bauxite samples was determined using powder X-Ray diffraction (XRD). For this study, the samples were powdered using an agate mortar and pestle, and were manually pressed by means of a glass plate to get a flat surface in cylindrical 16x2.5 mm sample holders. The diffractograms were obtained in a PANalytical X'Pert PRO MPD Alpha1 powder diffractometer in Bragg-Brentano h/2h geometry of 240 mm radius, nickel filtered Cu Ka radiation (k = 1.5418 Å), and with 45 kV–40 mA. During analysis, samples were spun at 2 revolutions per second. A variable divergence slit kept an area illuminated constant (10 mm) and a mask was used to limit the length of the beam (12 mm). Axial divergence Soller slits of 0.04 rad were used. Powdered samples were scanned from 4 to 80° 2θ with a step size of 0.017° and measuring time of 50 s per step, using a X'Celerator detector (active length = 2.122°). Sample preparation and analysis were performed in the Scientific and Technological Centres of the Universitat de Barcelona (CCiT-UB). Furthermore, one REE carbonate grain was manually hand-picked from a monolayer polished section and was analysed by monocrystal XRD. The monocrystal diffractometer used was a Bruker D8 Venture with a Mo source, a 4 circle goniometer with Kappa geometry, with a Photon 100 CMOS area detector, at a distance of 50 mm, and 2θ = Ω = Chi = 0°, Phi = 360°, in the CCiT-UB. The X-ray diffractograms were processed using the software X'Pert HighScore® (including background substraction, peak detection, mineral identification, and semiquantitative determination).

For the production of heavy mineral concentrates, 100 g of two homogenised bauxite samples, one from Aceitillar (sample AC-1–3) and another from El Turco (sample KM30-1) were processed at the hydroseparation (HS) laboratories available in the University of Barcelona (https://www.hslab-barcelona.com) and the Luleå University of Technology. The computer-controlled hydroseparation device CNT HS 11 was used (Rudashevsky and Rudashevsky, 2007; see also https://www.cnt-mc.ru) following the methodology for soft rocks proposed by

Table 1
List of the REE-bearing minerals analysed, and the method used for their corresponding structural formulae based on EMP analyses (apfu: atoms per formula unit).

Mineral	Abbreviation	Ideal formula	Structural formula calculation method
Monazite	Mnz	$REE(PO_4)$	O = 4
Xenotime	Xen	$Y(PO_4)$	O = 4
Churchite	Chc	$REE(PO_4)\cdot 2H_2O$	O = 4; $H_2O = 2*(P + Si)_{apfu}$
Rhabdophane	Rha	$REE(PO_4)\cdot H_2O$	O = 4; $H_2O = (P + Si)_{apfu}$
Bastnäsite	Bas	$REE(CO_3)(OH)$	$\sum REE + Y + Ga + Ca = 1; OH + F + Cl = 1; CO_3 = \sum REE + Y + Ga + Ca$

Aiglsperger et al. (2015). Heavy mineral concentrates from three size fractions (<30, 30– 75, and 75–125 μm) were further separated with a FRANTZ magnetic separator. Each separation product was embedded in resin to obtain cylindrical monolayer polished sections of 2.5 cm in diameter for subsequent investigation. A total of 116 REE mineral grains, 53 from El Turco and 63 from Aceitillar, were found in the dense mineral separates of the coarser size fractions (30–75 and 75–125 μm); of these, 57 grains were phosphates, and 59 were carbonates.

The mineralogy and textures of REE-bearing minerals were studied on monolayer polished sections, polished sections, and thin sections, by means of transmitted and reflected light petrographic microscopy and scanning electron microscopy. The scanning electron microscope (SEM) used was an Environmental SEM Quanta 200 FEI, XTE 325/D8395 equipped with an INCA Energy 250 EDS microanalysis system (operating conditions: acceleration voltage of 20 kV and a beam current of 1nA) at CCiT-UB. Chemical analyses of the REE-bearing minerals were performed using a JEOL JXA-8230 electron microprobe (EMP) also at the CCiT-UB, operated at 20 kV acceleration voltage, 15nA beam current, and a beam diameter of 5 μm. Analytical standards and lines used for analyses were: wollastonite (Si K α), apatite (Ca Kα, P Kα), barite (Ba Lα), celestine (Sr Lα), UO_2 (U Mβ), ThO_2 (ThMα), GaAs (Ga Lα), YAG (Y Lα), LaB6 (La Lα), CeO_2 (Ce Lα), REE-1 (Pr Lβ, Er Lα), REE-2 (Ho Lβ, Tm Lα, Eu Lα), REE-3 (Yb Lα, Sm Lβ, Gd Lα) and REE-4 (Lu Lα, Tb Lα, Nd Lβ). The structural formulae were calculated following the criteria described in Table 1.

Aqueous speciation and predominance Eh-pH diagrams to study REE mineral stability have been drawn with the code PhreePlot® (Kinniburg and Cooper, 2011) using the database llnl.dat supplied with the code PHREEQC (Parkhurst and Appelo, 2013) at 25 °C. This thermodynamic database contains equilibrium constants for aqueous speciation and mineral formation of major and minor elements. In the case of REE, llnl.dat database accounts for the formation of pure hydroxides, carbonates, and phosphates for most REE. However, data for churchite ($YPO_4\cdot H_2O$) was not included in the database and the equilibrium constant from Spahiu and Bruno (1995) for r.1 was used in calculations (Eq. (1)).

$$YPO_4\cdot xH_2O = Y^{3+} + PO_4^{3-} + xH_2O \qquad \log K^o = -22.4 \text{ r.1} \tag{1}$$

4. Results

4.1. Major and trace element composition

In the studied bauxite samples, Al and Fe are the elements with the highest concentrations. In El Turco, Al_2O_3 contents vary between 40 and 46 wt%, and Fe_2O_3 between 16 and 19 wt%. In Aceitillar, Al_2O_3 contents are between 35 and 50 wt%, and Fe_2O_3 between 15 and 21 wt%. In both deposits, SiO_2 contents are below 2 wt%. CaO values are below 1 wt% in both deposits, except for one sample from Aceitillar reaching 13 wt%. MnO contents are contrasting in samples from both deposits, with values of 2–7 wt% in El Turco and <1 wt% in Aceitillar. In El Turco and Aceitillar, P_2O_5 is up to 4 wt% and 1 wt%, respectively. Based on the major element composition (Bárdossy, 1982), samples from El Turco and Aceitillar can be classified as iron-rich bauxites (Fig. 3), like bauxite

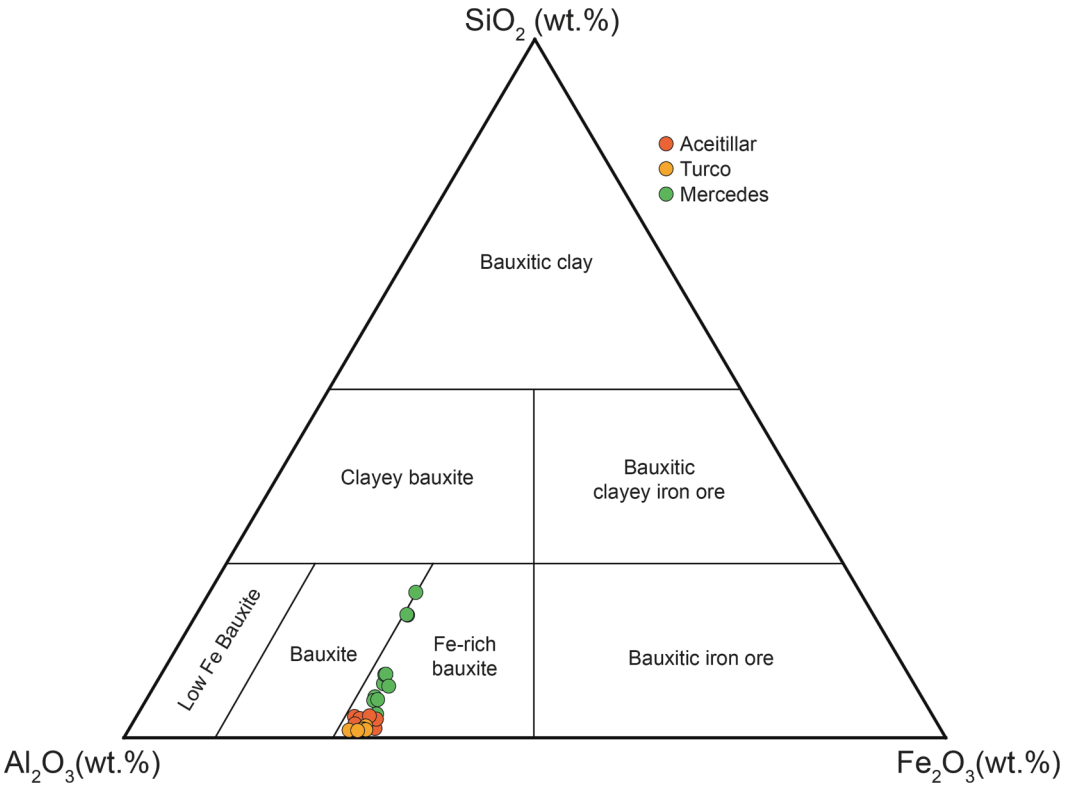

Fig. 3. Geochemical classification of the studied karst bauxite deposits from Sierra de Bahoruco. Compositional fields are after Bárdossy (1982).

Table 2
REE geochemistry of selected bulk samples from El Turco and Aceitillar (analyses in ppm).

Deposit	Sample	Y	La	Ce	Pr	Nd	Sm	Eu	Gd	Tb	Dy	Ho	Er	Tm	Yb	Lu	Sum REY
El Turco	Km30-1-2019-2	14,830	399	330	166	2320	1270	439	2870	453	2590	496	1320	169	990	145	28,787
El Turco	Km30-1-2019-2A	12,580	613	358	334	3000	985	264	1630	262	1600	348	965	119	677	104	23,839
Aceitillar	AC1-P1-2	1068	254	305	45	207	61	16	74	13	85	19	51	6	39	5	2248
Aceitillar	AC1-P1-3	1303	228	311	38	171	90	33	162	33	214	40	109	16	103	15	2866

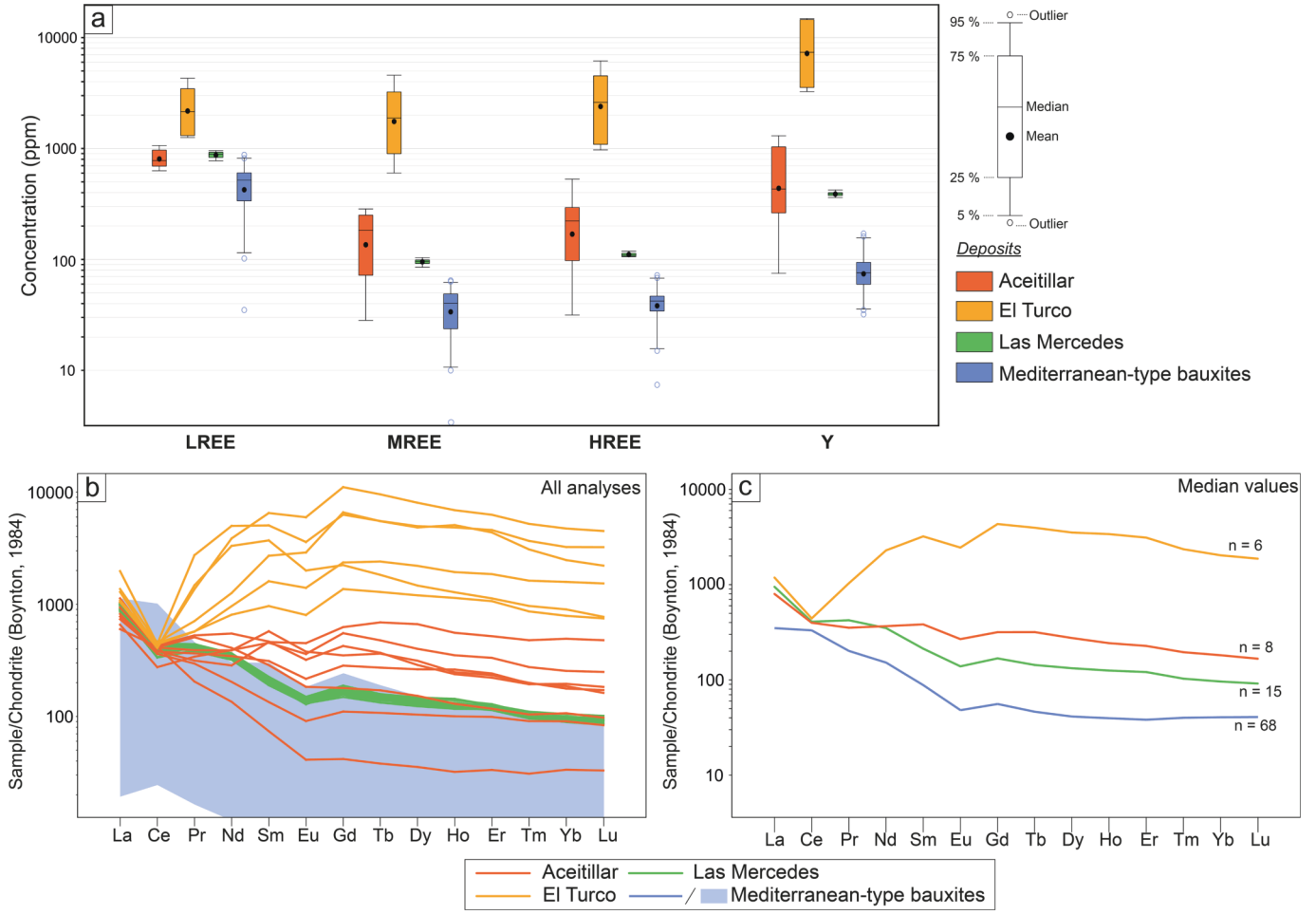

Fig. 4. a) box and whiskers plot for lree (la-nd), mree (sm-gd), hree (tb-lu), and y; b) chondrite-normalised ree plot for whole rock data from the studied deposits; c) chondrite-normalised ree plot of the median values from diagram b). Normalisation values in (b) and (c) are after Boynton (1984). Shown for comparison are data from Las Mercedes (Torró et al., 2017) and Mediterranean-type bauxites (Mondillo et al., 2011, 2019; Deady et al., 2014; Mouchos et al., 2016; Putzolu et al., 2018; Reinhardt et al., 2018; Radusinović and Papadopoulos, 2021).

ore from Las Mercedes (Torró et al., 2017). Elements at minor and trace levels include TiO_2 (<3 wt%), Ni (1,320–6,960 ppm in El Turco and 200–660 ppm in Aceitillar), Cr (<850 ppm), Zr (<515 ppm), Sc (<75 ppm), Ga (<50 ppm), and Ge (<6 ppm).

The analysed samples from El Turco and Aceitillar yield very high REY (La-Lu + Y) contents. Samples from El Turco are particularly enriched in these elements, with REY contents up to 2.88 wt% and an average value of 1.64 wt% (Table 2). In samples from Aceitillar, REE + Y contents are up to 2,865 ppm, with an average value of 1,810 ppm.

Samples from El Turco have average contents of LREE (La-Nd), MREE (Sm-Gd), and HREE (Tb-Lu) between ~2,000 to 3,000 ppm each, and Y contents reach 8,841 ppm (Fig. 4a). They are enriched between 1,000 and 10,000 times relative to chondritic values. In chondrite-normalised diagrams, these samples are characterized by notable dispersion and very irregular patterns with systematic negative anomalies of Ce, common negative Eu anomalies, and conspicuous enrichment in MREE and HREE relative to LREE (Fig. 4b-c).

The samples from Aceitillar have LREE, MREE, HREE, and Y average contents between ~120 and ~800 ppm. They are enriched ~1,000 times in LREE and ~200 to 300 times in MREE and HREE relative to the chondritic values thus showing negative slopes in chondrite-normalised REE patterns (Fig. 4b-c). Most samples from Aceitillar have moderate negative anomalies of Ce and Eu (Fig. 4c).

4.2. General mineralogy of the bauxite and phosphate-vein samples

Powder XRD analyses indicate that bauxite samples consist mainly of gibbsite [$Al(OH)_3$], with lesser amounts of hematite [Fe_2O_3], boehmite [AlO(OH)], goethite [$Fe^{3+}O(OH)$], anatase [TiO_2], and rutile [TiO_2] (Fig. 5a-b). In addition, minor amounts of lithiophorite-asbolane [$(Al,Li)MnO_2(OH)_2$-$(Ni,Co)_{2-x}Mn(O,OH)_4{\cdot}nH_2O$] and florencite [$REEAl_3(PO_4)_2(OH)_6$] have been identified in the sample from El Turco (Fig. 5b).

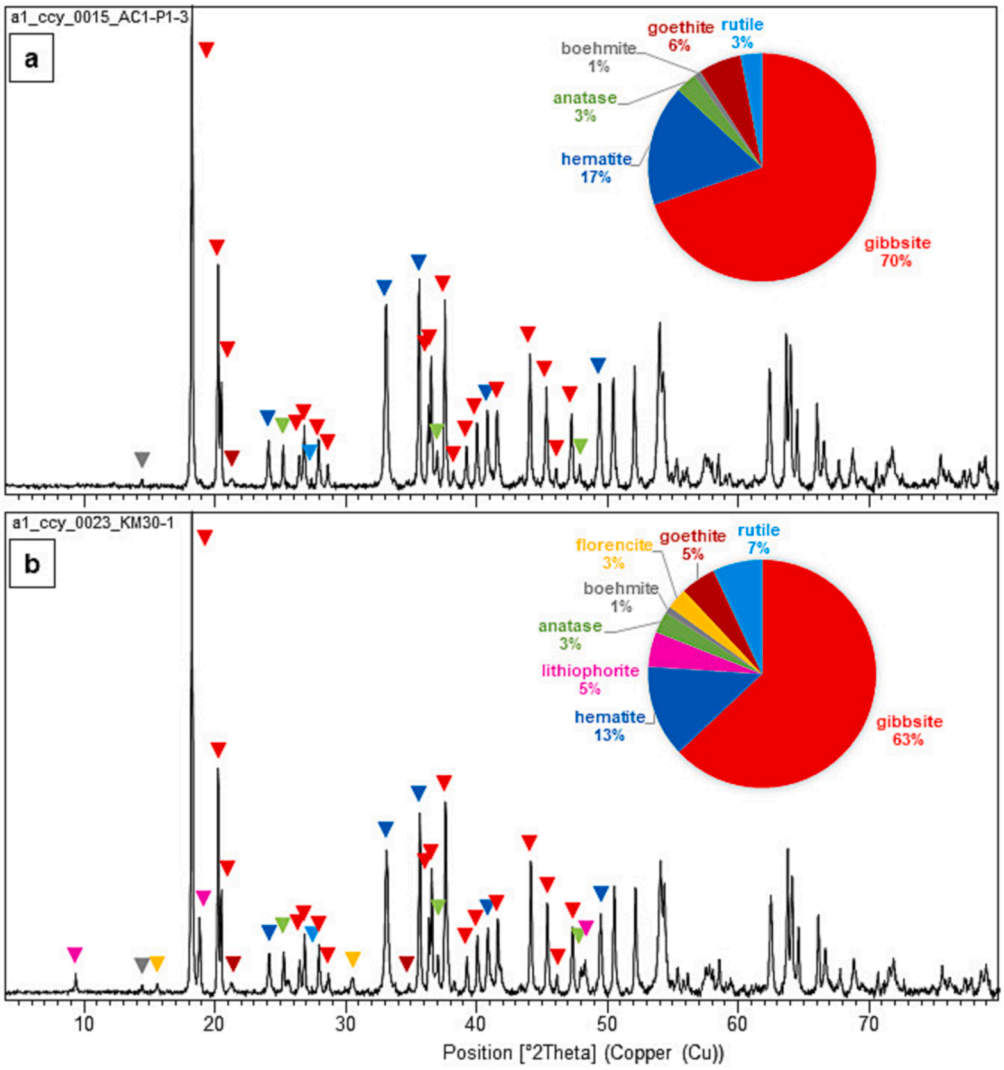

Fig. 5. Powder X-ray diffractograms of the two samples that subsequently underwent sieving, hydroseparation, and Frantz magnetic separation: a) Aceitillar (sample AC-1–3), and b) El Turco (sample KM30-1). Mineral identification of the peaks (of the first 50° 2θ) is marked with triangles (colours correspond with the pie diagrams).

The main mineralogy is very similar to that reported by Torró et al. (2017) in the nearby Las Mercedes deposit. The predominance of gibbsite and the scarcity of kaolinite, or lack thereof, indicate a mature profile, representative of an advanced state of bauxitization (see also Torró et al., 2017; Proenza et al., 2017; Villanova-de-Benavent et al., 2017).

Furthermore, one sample from the yellowish vein infilling in bauxites from El Turco (Fig. 2f) was also analysed by powder XRD. The vein material consists mostly of xenotime, with minor gibbsite and traces of lithiophorite-asbolane and florencite (Fig. 6).

4.3. Detailed REE mineralogy

In the study area, REE-bearing minerals are divided into phosphates and carbonates. According to textural features, phosphates may be in turn sub-divided into primary (relict) and secondary (authigenic).

Primary phosphates are monazites, which occurs as individual grains up to 60 μm in length. Most of them are euhedral (Fig. 7a), but some exhibit slightly rounded edges and/or irregular, fractured outlines that suggest transport (Fig. 7b-d). Melt inclusions are common in some monazite grains (Fig. 7e). Most EMP analyses of primary monazite show analytical oxide totals close to 100 wt% and near ideal stoichiometry (both A and B site cations have total ~1 a.p.f.u.; Table 3). All monazites from El Turco and Aceitillar classify as monazite-(Ce) except for one grain from El Turco that has a monazite-(La) composition (Fig. 7f). Monazite-(Ce) contains 27.5–33.3 wt% Ce_2O_3 (average of 30.6 wt%), 11.2–20.0 wt% La_2O_3 (average of 15.9 wt%), and 9.6–13.4 wt% Nd_2O_3 (average of 10.7 wt%). They also yield notable Pr (2.3–3.4 wt%, average 2.7 wt% Pr_2O_3) and Gd (1.0–3.6 wt%, average of 2.6 wt% Gd_2O_3) contents. Y_2O_3, Sm_2O_3, Eu_2O_3, Dy_2O_3, and Tm_2O_3 are mostly below 1 wt % each, and Tb_2O_3, Ho_2O_3, Er_2O_3, Yb_2O_3, and Lu_2O_3 are below their respective lower limits of detection. As expected, analysed monazites yield much higher ThO_2 (2.1–10.7 wt%, average of 4.7 wt%), than UO_2 (<d.l.-1.2 wt%, average of 0.4 wt%). CaO contents are up to 1.2 wt% (average of 0.7 wt%; Table 3). Primary relict monazite-(Ce) from El Turco and Aceitillar present similar textures and compositions to those of Las Mercedes (Fig. 7g), where this phosphate constitutes the main REE-phase in heavy concentrates of bauxite ore (Torró et al., 2017).The monazite-(La) grain contains 26.6 wt% La_2O_3, 17.0 wt% Nd_2O_3, 4.8 wt% Sm_2O_3, 3.8 wt% Pr_2O_3, 2.7 wt% Gd_2O_3, 1.4 wt% Y_2O_3, the rest of the REE below 1.0 wt% REE_2O_3, and 9.8 wt% CaO.

Based on EMP analyses, secondary REE phosphates are anhydrous (possibly xenotime [$REE(PO_4)$]) to hydrated (possibly rhabdophane [$REE(PO_4)\cdot H_2O$] and/or churchite [$REE(PO_4)\cdot 2H_2O$]), all with a $\sum$REY: PO_4 ratio of 1:1. However, it must be noted that some analyses were slightly non stoichiometric, and data with high Al_2O_3 were not

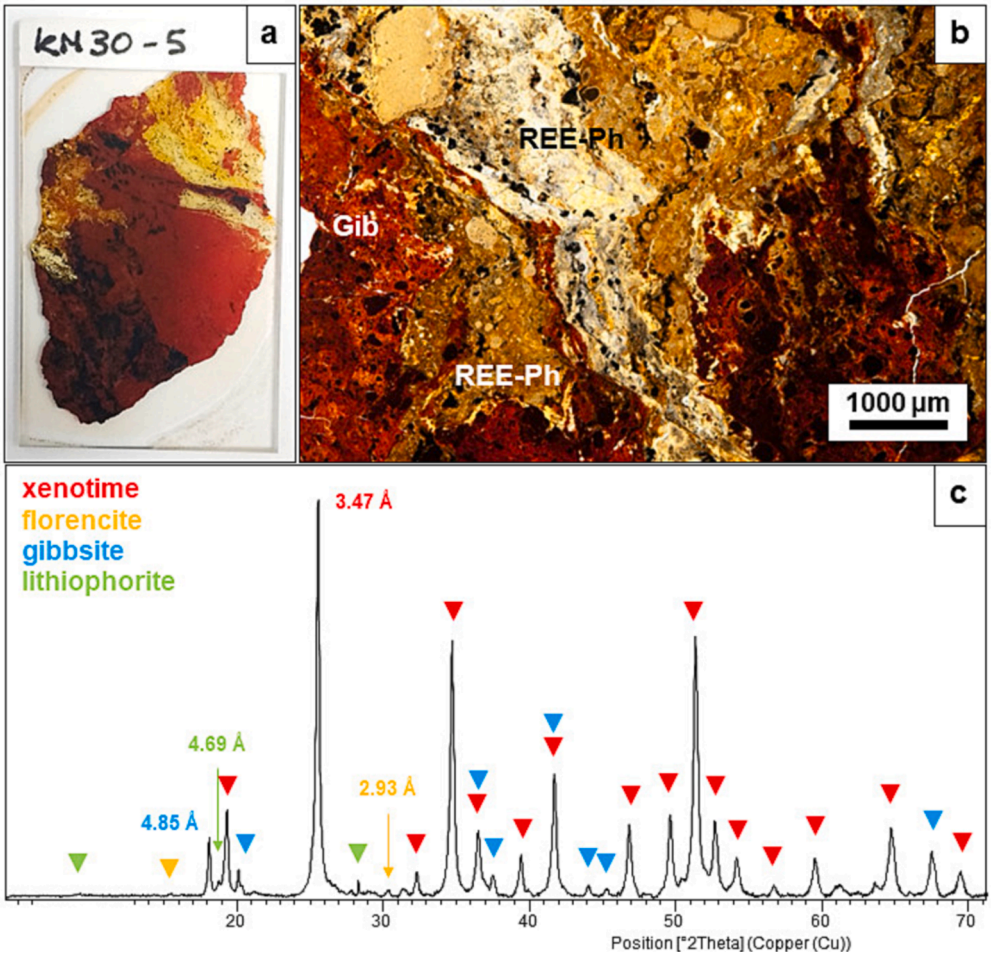

Fig. 6. REE-rich sample KM30-5 from El Turco: a) photograph of the polished thin section, where the yellow REE-phosphate can be observed, surrounded by the reddish-brown Fe-rich gibbsite and some black Mn oxyhydroxides (length of the glass slide is 4.5 cm); b) plane polarised light photomicrograph of the REE-phosphate (REE-Ph) veinlet crosscutting the gibbsite (Gib) matrix; c) powder X-ray diffractogram of the yellow REE-phosphate (the labelled peaks represent the most intense d_{hkl} of the identified minerals).

considered for this study since they were probably contaminated by nearby gibbsite. Secondary REE phosphates display a wide variety of textural features, most notably as porous vein infillings crosscutting the gibbsite matrix; they consist of rounded, submicrometric free grains or micrometric aggregates finely intergrown with gibbsite (Fig. 8a). Submicrometric grains may agglomerate in larger porous clusters (Fig. 8a-b). In numerous areas of the studied samples, secondary REE phosphates occur as fine coatings on rounded micrometric (Fig. 8c) to millimetric Mn oxyhydroxide grains (Fig. 8d-e). In addition, they also form angulous grains with large pores (Fig. 8f), subrounded, homogeneous, irregular-shaped grains of tens of micrometres in length (Fig. 8g-h). Although EMP analyses revealed that Y is, by far, the main REE, some datapoints yield Nd as the dominant REE. The analysed secondary REE phosphates contain 2.3–50.3 wt% Y_2O_3 (average of 32.6 wt%), and up to 38.54 wt% Nd_2O_3 (average of 1.0 wt%), 10.0 wt% Sm_2O_3 (average of 1.1 wt%), 11.0 wt% Gd_2O_3 (average of 6.2 wt%), and 10.2 wt% Dy_2O_3 (average of 5.8 wt%). Pr_2O_3, Eu_2O_3, Er_2O_3, and Yb_2O_3 contents are below 5 wt%, and La_2O_3, Ce_2O_3, Tb_2O_3, Ho_2O_3, Tm_2O_3, and Lu_2O_3 contents are below 2 wt% (Fig. 9, Table 4). Results of a few analyses include high Al_2O_3 contents (average 31.0 wt%) and Nd and Sm as the dominant REE cations (12.5 wt% Nd_2O_3 and 4.5 wt% Sm_2O_3), but are REE-deficient (23.1 wt% total $REE_2O_3 + Y_2O_3$) compared with the typical florencite composition (analysed grain shown in Fig. 8f). Hence, even though florencite (or a florencite-like structure) was detected by powder XRD, representative analyses could not be obtained.

The REE carbonates belong to the bastnäsite group. They have been observed as individual free grains composed of porous and/or fragmented aggregates (Fig. 10a). In these aggregates, rod-shaped particles can be commonly distinguished (Fig. 10b). Some aggregates display concentric zoning (Fig. 10c) or more convolute internal heterogeneities (Fig. 10d). In terms of chemical composition, they fall within the so-called bastnäsite [$REE(CO_3)(F,OH)$]-synchysite [$CaREE(CO_3)_2(F,OH)$] polysomatic mineral series (Zeug et al., 2021 and references therein). Their main feature is that the dominant REE is mostly Gd (Fig. 10a-d) and less commonly, Nd (Fig. 10e-f). They contain 4.8–38.8 wt% Gd_2O_3 (average of 26.1 wt%), 4.1–40.1 wt% Nd_2O_3 (average of 12.8 wt%) and 4.6–19.0 wt% Sm_2O_3 (average of 10.6 wt%), <10 wt% La_2O_3, Pr_2O_3, Eu_2O_3, Tb_2O_3, Dy_2O_3, and Y_2O_3, and less than 2 wt% Ho_2O_3, Er_2O_3, Tm_2O_3, Yb_2O_3, and Lu_2O_3. Cerium is below its lower limit of detection (Table 5). Since Ca is below 5.6 wt% (average of 1.7 wt%) and F is below its lower limit of detection, the datapoints plot closer to the bastnäsite end-member (*vs.* synchysite composition; Fig. 10g) and hence the name hydroxylbastnäsite is more appropriate. If so, and pending further crystallographical or structural evidence, this would be the first description of a natural Gd-dominated carbonate. Nevertheless, monocrystal XRD on one hand picked Gd-dominant carbonate grain gave a calcioancylite [$CaREE(CO_3)_2(OH)\cdot(H_2O)$] structure, which indicates that the mineralogy of REE carbonates from bauxites in Bahoruco might be particularly complex and requires more detailed and systematic crystallochemical studies (Fig. 11).

While monazite can be found in similar proportions in both deposits, secondary phosphates are more abundant in El Turco, and the secondary carbonates are exclusive of Aceitillar. In addition, two grains of apatite have been found in heavy concentrates in samples from El Turco. The observed apatite grains are subhedral, poorly rounded, and have a porous appearance; they do not have significant REE contents. Noteworthy, cerianite [CeO_2], which was documented in the Las Mercedes deposit (Torró et al., 2017), was not observed in the studied samples

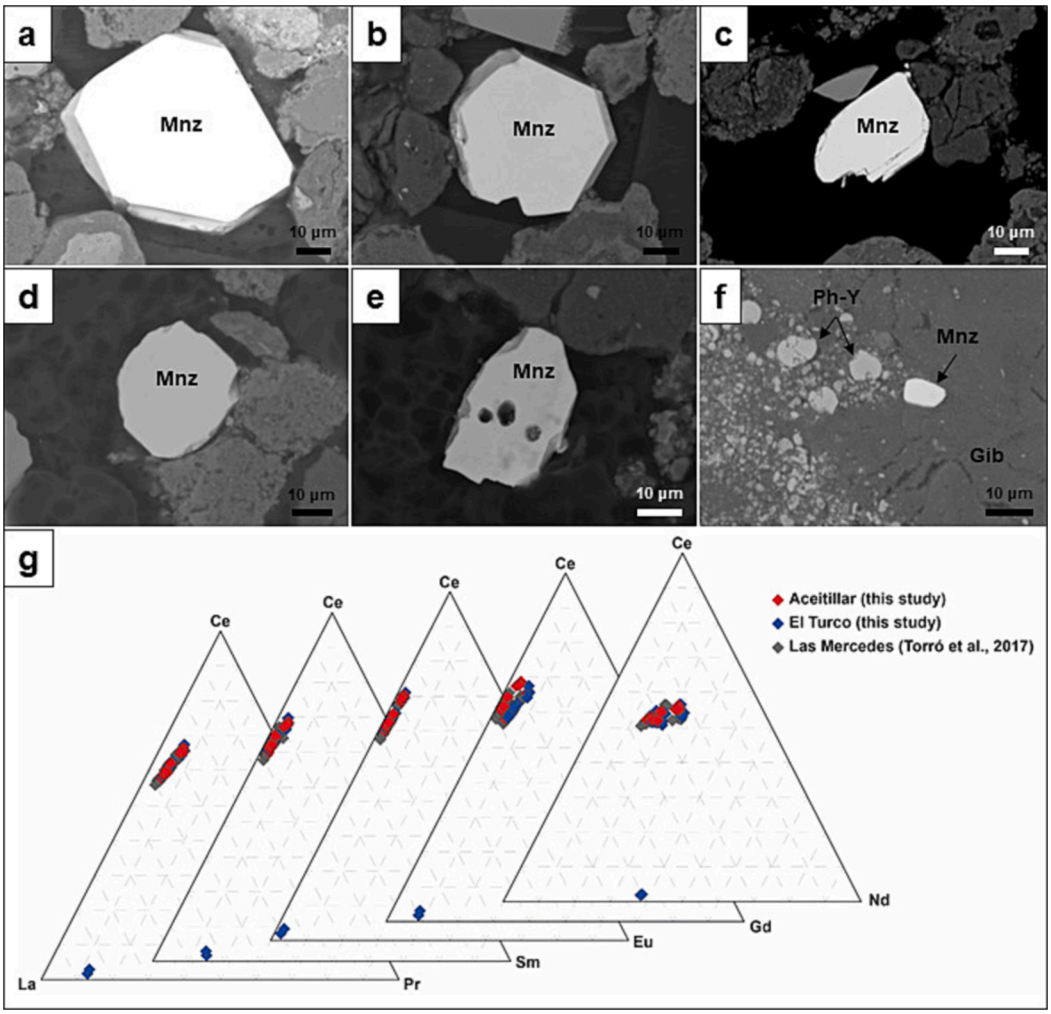

Fig. 7. Textures and mineral chemistry of primary monazites from El Turco and Aceitillar: a-f) SEM backscattered electron (BSE) images of monazite-(Ce) from El Turco (a-c) and Aceitillar (d-e), and monazite-(La) from El Turco (f); g) ternary plots depicting the REE compositions of the monazite grains from El Turco and Aceitillar (this study). Compositional data of monazite(-Ce) from the Las Mercedes deposit after Torró et al. (2017) is also shown for comparison. Abbreviations: Mnz = monazite, Gib = gibbsite, Ph-Y = secondary Y phosphate.

from the El Turco and Aceitillar deposits.

5. Discussion

5.1. The mineralogical nature of REE ores in Sierra de Bahoruco

The most typical REE minerals identified in bauxite deposits worldwide include cerianite, parisite, röntgenite, synchysite-(Nd), rhabdophane, churchite, bastnäsite-(Ce), bastnäsite-(Nd), hydroxylbastnäsite-(Nd, La), hydroxylcarbonate-(Nd, La), xenotime, monazite-(La), and monazite-(Nd) (Ochsenkühn-Petropulu and Ochsenkühn, 1995; Lymperopoulou, 1996; Maksimović and Pantó, 1996, 1991; Mongelli, 1997; Pantó and Maksimović, 2001; Laskou et al., 2003; Mameli et al., 2007; Wang et al., 2010; Gamaletsos et al., 2011; Li et al., 2013; Liu et al., 2016; Kalatha et al., 2017). REE minerals in bauxite deposits are originated by accumulation of residual (primary) phases, precipitation (neoformation), and adsorption of ions onto mineral surfaces (mostly clay minerals) (Deady et al., 2014 and references therein). The REE minerals identified in bauxites from the Pedernales Peninsula are both relict and authigenic. On one hand, as in many other karst-bauxite deposits, the main detrital REE-mineral is monazite-(Ce, La) (Maksimović and Pantó, 1996). The presence of monazite grains results in high LREE values in the studied bauxite ores. We interpreted that monazite grains were transported into karstic pockets and survived the bauxitisation process (Maksimović and Pantó, 1991; Mondillo et al., 2011). On the other hand, authigenic REE-phosphates and REE-carbonates evidence REE mobilisation and redeposition during the bauxitisation process as vein infillings crosscutting the gibbsite matrix and/or coatings on other grains. Specifically, the secondary REE-bearing phases can be grouped into: i) anhydrous and hydrated, Y-dominated phosphates with a ratio REE:PO_4 of 1:1 (possibly xenotime, rhabdophane, and/or churchite), and ii) Gd-dominated carbonates of the bastnäsite group (precisely hydroxylbastnäsite-(Gd)) (Figs. 7, 8 and 10).

It is noteworthy that hydroxylbastnäsite-(Nd) is commonly described as the most common authigenic REE mineral in karst-bauxite according to Deady et al. (2014). However, hydroxylbastnäsite from bauxite deposits in Bahoruco concentrate preferentially Gd. Therefore, the existence of new mineral species or varieties of REE minerals in Sierra de Bahoruco is plausible and further, on-going work is required for their correct crystallochemical characterization.

The mineralogical differences on the authigenic REE phases found in the two bauxite deposits studied here are conspicuous. While REE-phosphates are characteristic of El Turco, REE-carbonates are only found in Aceitillar translating also in distinctive contents of particular rare earth elements. Importantly also, the contrast between the main REE in primary (Ce, La) *vs.* secondary (Y, Nd) phosphates and carbonates (Gd, Nd) requires consideration of an additional source of REE for the secondary phosphates and carbonates, other than the primary

Table 3
Representative EMP analyses of primary relict monazite grains from El Turco and Aceitillar. Cations are normalised to 4 oxygens (n.a. = not analysed, d.l. = below detection limit).

Label	690	694	701	706	709	712	665	669	673	679	680	684
Deposit	El Turco	El Turco	El Turco	El Turco	El Turco	El Turco	Aceitillar	Aceitillar	Aceitillar	Aceitillar	Aceitillar	Aceitillar
P_2O_5 (wt.%)	30.89	29.53	30.33	30.12	30.3	29.47	30.2	29.62	30.02	30.51	30.53	30.56
SiO_2	d.l.	d.l.	d.l.	d.l.	d.l.	d.l.	0.85	d.l.	d.l.	d.l.	d.l.	0.43
TiO_2	n.a.	n.a.	n.a.	n.a.	n.a.	n.a.	n.a.	n.a.	n.a.	n.a.	n.a.	n.a.
CaO	0.67	0.58	0.40	0.60	0.62	0.38	0.73	1.18	0.41	0.85	0.90	1.02
BaO	d.l.	d.l.	0.11	d.l.	d.l.	d.l.	d.l.	d.l.	d.l.	d.l.	d.l.	d.l.
SrO	d.l.	d.l.	d.l.	0.09	d.l.	d.l.	d.l.	0.13	d.l.	d.l.	d.l.	0.15
UO_2	0.36	d.l.	d.l.	0.25	0.18	d.l.	0.45	d.l.	d.l.	d.l.	d.l.	0.47
ThO_2	3.11	4.55	3.72	4.10	5.30	4.60	6.11	4.62	4.94	4.06	3.75	3.74
Ga_2O_3	d.l.	d.l.	d.l.	d.l.	d.l.	0.08	0.15	d.l.	0.08	d.l.	d.l.	d.l.
Y_2O_3	0.43	0.37	0.50	0.79	0.47	0.38	0.52	0.40	0.34	0.43	0.44	0.41
La_2O_3	12.21	16.68	17.53	15.48	16.42	18.55	12.19	15.70	16.93	16.33	15.87	17.15
Ce_2O_3	29.77	30.76	30.90	30.40	30.26	30.35	29.16	30.75	30.27	30.98	30.57	30.81
Pr_2O_3	3.32	2.64	2.76	2.56	2.40	2.60	2.85	2.92	2.45	2.55	2.87	2.53
Nd_2O_3	13.25	10.08	10.17	10.65	9.65	9.72	11.28	9.89	10.14	10.29	10.48	9.82
Sm_2O_3	1.75	0.55	0.68	0.94	0.64	0.62	1.43	0.59	0.64	0.63	0.66	0.58
Eu_2O_3	0.73	0.40	0.47	0.53	0.48	0.47	0.52	0.50	0.40	0.52	0.46	0.41
Gd_2O_3	3.47	2.81	2.72	2.95	2.76	2.81	3.14	2.89	2.83	2.70	2.85	2.80
Tb_2O_3	d.l.	d.l.	d.l.	d.l.	d.l.	d.l.	d.l.	d.l.	d.l.	d.l.	d.l.	d.l.
Dy_2O_3	0.30	d.l.	0.20	0.22	0.14	d.l.	0.30	0.28	d.l.	d.l.	0.14	d.l.
Ho_2O_3	d.l.	d.l.	d.l.	d.l.	d.l.	d.l.	d.l.	d.l.	d.l.	0.22	0.11	d.l.
Er_2O_3	d.l.	d.l.	d.l.	d.l.	d.l.	d.l.	d.l.	d.l.	d.l.	d.l.	d.l.	d.l.
Tm_2O_3	0.21	0.11	d.l.	0.19	0.13	0.10	0.19	0.15	d.l.	d.l.	d.l.	d.l.
Yb_2O_3	d.l.	d.l.	d.l.	d.l.	d.l.	d.l.	d.l.	d.l.	d.l.	d.l.	d.l.	d.l.
Lu_2O_3	d.l.	d.l.	d.l.	d.l.	d.l.	d.l.	d.l.	d.l.	0.07	d.l.	d.l.	d.l.
Total	100.46	99.06	100.50	99.88	99.76	100.13	100.08	99.62	99.51	100.07	99.63	100.87
P (a.p.f.u)	1.029	1.017	1.020	1.022	1.032	1.011	1.021	1.014	1.026	1.025	1.026	1.015
Si	–	–	–	–	–	–	0.034	–	–	–	–	0.017
Sum B	1.029	1.017	1.020	1.022	1.032	1.011	1.055	1.014	1.026	1.025	1.026	1.032
Ca	0.028	0.025	0.017	0.026	0.027	0.017	0.031	0.051	0.018	0.036	0.038	0.043
Ba	–	–	0.002	–	–	–	–	–	–	–	–	–
Sr	–	–	–	0.002	–	–	–	0.003	–	–	–	0.003
U	0.003	–	–	0.002	0.002	–	0.004	–	–	–	–	0.004
Th	0.028	0.042	0.034	0.037	0.049	0.042	0.056	0.043	0.045	0.037	0.034	0.033
Ga	–	–	–	–	–	0.002	0.004	–	0.002	–	–	–
Y	0.009	0.008	0.011	0.017	0.010	0.008	0.011	0.009	0.007	0.009	0.009	0.009
La	0.177	0.250	0.257	0.229	0.244	0.277	0.180	0.234	0.252	0.239	0.232	0.248
Ce	0.429	0.458	0.449	0.446	0.446	0.450	0.427	0.455	0.448	0.450	0.444	0.443
Pr	0.048	0.039	0.040	0.037	0.035	0.038	0.041	0.043	0.036	0.037	0.041	0.036
Nd	0.186	0.146	0.144	0.152	0.139	0.141	0.161	0.143	0.146	0.146	0.149	0.138
Sm	0.024	0.008	0.009	0.013	0.009	0.009	0.020	0.008	0.009	0.009	0.009	0.008
Eu	0.010	0.005	0.006	0.007	0.007	0.006	0.007	0.007	0.005	0.007	0.006	0.005
Gd	0.045	0.038	0.036	0.039	0.037	0.038	0.042	0.039	0.038	0.036	0.037	0.036
Tb	–	–	–	–	–	–	–	–	–	–	–	–
Dy	0.004	–	0.003	0.003	0.002	–	0.004	0.004	–	–	0.002	–
Ho	–	–	–	–	–	–	–	–	–	0.003	0.001	–
Er	–	–	–	–	–	–	–	–	–	–	–	–
Tm	0.003	0.001	–	0.002	0.002	0.001	0.002	0.002	–	–	–	–
Yb	–	–	–	–	–	–	–	–	–	–	–	–
Lu	–	–	–	–	–	–	–	–	0.001	–	–	–
Sum A	0.993	1.022	1.008	1.014	1.006	1.030	0.989	1.040	1.007	1.007	1.004	1.007

phosphates. Information on the REE mineralogy related to karst bauxites being limited yet, we focus in the following lines on the stability of authigenic REE minerals and constraints on their behaviour during the bauxitisation process.

It must be noted that no textural relationships were observed between primary and secondary REE phosphates, between REE phosphates and REE carbonates, and between REE-carbonates and REE-free carbonates.

5.2. Mineral stability of REE phosphates and carbonates

Predominance diagrams shown in Fig. 12 summarise the stability fields of the major minerals identified in the deposits of Aceitillar and El Turco. In Aceitillar, the presence of gibbsite, kaolinite and hematite, together with calcite suggests that groundwaters should be alkaline (pH in the range 8–10); the fact that no Mn minerals have been identified would, in addition, indicate that such groundwaters were not very oxidant (Eh $<$ 0.5 V). In Aceitillar, REE phases are mainly carbonate minerals, whose stability field is close to the equilibrium of calcite and agrees with equilibrium between kaolinite and gibbsite (Fig. 12, left). In El Turco, however, as Mn oxides have been identified, Eh conditions should be more oxic than in Aceitillar (Eh $>$ 0.5 V; Fig. 12, right). Neither kaolinite nor calcite are present at El Turco, and REE-bearing minerals are mainly secondary phosphates. The stability field of these minerals is located at more acidic pH than REE-bearing carbonate minerals, and considering the Eh restrictions defined by Mn-oxides, the Eh-pH conditions of El Turco are lower pH and higher Eh relative to those of Aceitillar.

Concerning aqueous speciation, REE as free cations are the most important species at pH lower than 6, even when fluoride ion is present, and hydroxyl compounds prevail at pH higher than 11. The pH range between 6 and 11 is dominated by carbonate and phosphate aqueous

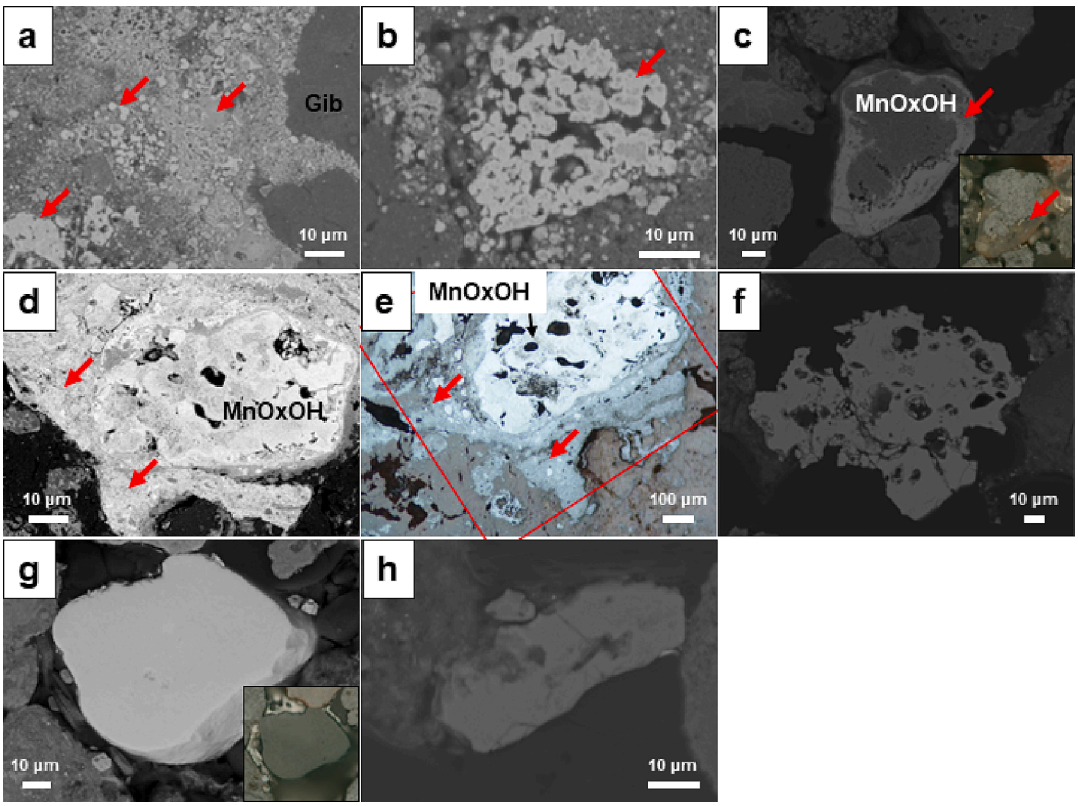

Fig. 8. Backscattered electron (BSE) images (a-d, f-h) and reflected light optical micrographs (e, and insets in c and g) of secondary REE-phosphate grains identified in the karst bauxites of Sierra de Bahoruco: a-b) hydrated Y-phosphate grains and aggregates as vein infillings within the gibbsite matrix (Gib), c-e) anhydrous (c) and hydrated (d-e) Y-phosphate coating a Mn oxyhydroxide grain (MnOxOH), f) hydrated Y-phosphate grain with large pores, g) hydrated Y-phosphate subrounded grain, h) fragmented, irregular-shaped, hydrated Al-bearing Nd-phosphate grain. Red arrows mark the REE-phosphates in Fig. 8a-e. Fig. 8f was taken in a sample from Aceitillar, the others are from El Turco.

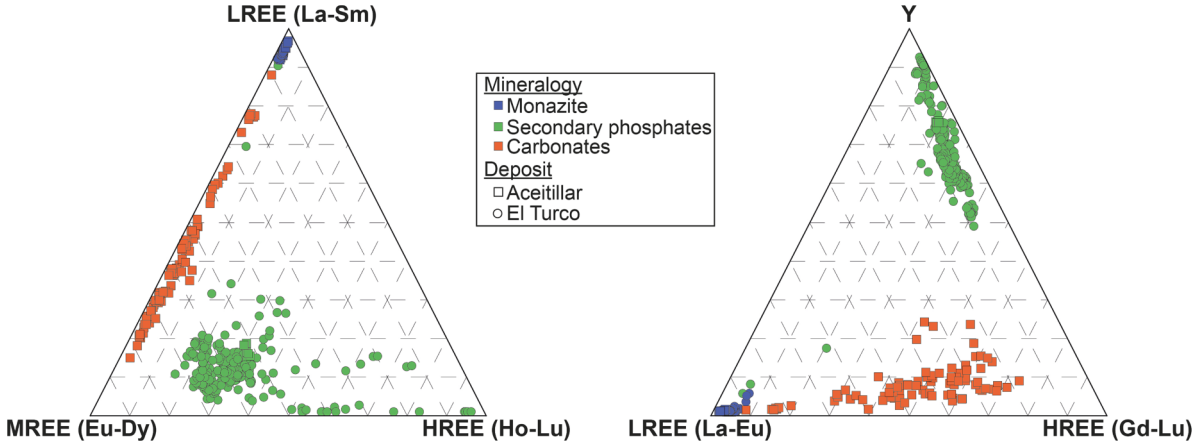

Fig. 9. Ternary plots depicting the composition of REE-bearing minerals (monazite, secondary phosphates and carbonates) from Sierra de Bahoruco karst bauxites in terms of LREE (La, Ce, Pr, Nd, Sm)-MREE (Eu, Gd, Tb, Dy)-HREE (Ho, Er, Tm, Yb, Lu) (left) and Y-LREE (La, Ce, Pr, Nd, Sm, Eu)-HREE (Gd, Tb, Dy, Ho, Er, Tm, Yb, Lu) (right), as obtained by EMP.

complexes, being the distribution highly dependent on the concentration of total carbonate and phosphate in groundwater. Thus, although the tendency of carbonate aqueous species of being formed is lower than phosphate ones, they are the dominant species at neutral-basic pH, because the carbonate aqueous concentration is usually higher than the phosphate aqueous concentration in groundwater. Phosphate aqueous species only appear at low pH, where carbonate is not stable, or in groundwaters richer in phosphate compared to carbonate.

The predominance of Al oxyhydroxides (gibbsite) and the insignificant amounts of kaolinite reveal a mature profile, characteristic of later stages of bauxitisation (Gu et al., 2013). During advanced bauxitisation, pH and Eh in the profile evolve towards more acidic and oxidising conditions, respectively. Those changes in pH and Eh would favour the dissolution of REE carbonates, formed during the initial stages, and the remobilisation of REE (Li et al., 2013). REE in solution (as free ions or forming organic acid or phosphate complexes) could precipitate as REE phosphates (e.g., rhabdophane, churchite and florencite) (Liu et al., 2016). This behaviour is coherent with the

Table 4
Representative EMP analyses of REE-phosphates from the Sierra de Bahoruco bauxite deposits (n.a.: not analysed; d.l.: below detection limit). FeOt: total Fe, H_2O is calculated according to Table 1.

Label	461	466	486	491	497	505	516	521	1020	1021	1026	1029
Deposit	**El Turco**	**El Turco**	**El Turco**	**El Turco**	**El Turco**	**El Turco**	**El Turco**	**El Turco**	**El Turco**	**El Turco**	**Aceitillar**	**Aceitillar**
P_2O_5 (wt.%)	24.23	29.64	24.77	27.92	28.75	23.95	29.08	27.34	26.11	26.46	27.11	25.54
SiO_2	2.11	1.54	1.60	2.35	1.83	0.65	1.57	1.57	1.80	1.30	2.60	2.59
TiO_2	0.25	d.l.	d.l.	0.17	d.l.	d.l.	d.l.	0.25	n.a.	n.a.	n.a.	n.a.
Al_2O_3	1.04	0.13	0.29	0.35	0.15	0.10	0.21	4.31	0.62	0.26	0.25	0.30
MnO	0.61	0.41	0.37	1.15	0.25	0.16	d.l.	d.l.	n.a.	n.a.	n.a.	n.a.
FeOt	2.62	0.63	0.70	0.84	0.15	d.l.	0.18	0.45	0.61	0.14	d.l.	0.08
NiO	d.l.	d.l.	d.l.	d.l.	d.l.	0.10	d.l.	d.l.	n.a.	n.a.	n.a.	n.a.
CaO	0.79	2.02	0.86	1.03	1.78	1.70	1.39	1.18	0.97	0.86	1.14	0.90
ThO_2	n.a.	n.a.	n.a.	n.a.	n.a.	n.a.	n.a.	n.a.	d.l.	d.l.	d.l.	d.l.
Ga_2O_3	d.l.	d.l.	d.l.	d.l.	d.l.	0.55	d.l.	d.l.	n.a.	n.a.	n.a.	n.a.
Y_2O_3	29.53	39.28	31.75	35.02	32.01	2.33	48.80	34.37	34.53	33.62	40.29	39.97
La_2O_3	d.l.	d.l.	d.l.	d.l.	d.l.	0.90	d.l.	d.l.	d.l.	0.20	d.l.	d.l.
Ce_2O_3	0.25	d.l.	d.l.	0.10	d.l.	d.l.	d.l.	d.l.	0.16	0.14	0.14	0.13
Pr_2O_3	d.l.	d.l.	d.l.	d.l.	d.l.	3.34	d.l.	d.l.	d.l.	d.l.	d.l.	d.l.
Nd_2O_3	0.79	0.21	1.01	0.61	1.09	38.54	0.12	0.22	1.17	1.16	1.63	1.52
Sm_2O_3	2.47	0.61	3.09	2.59	1.57	9.98	d.l.	0.63	3.80	3.81	1.37	1.45
Eu_2O_3	1.34	0.29	1.28	1.34	0.91	1.91	d.l.	0.28	1.78	1.84	0.61	0.58
Gd_2O_3	10.04	2.95	8.90	8.73	7.68	1.90	0.72	2.75	9.89	10.36	4.50	4.36
Tb_2O_3	1.10	0.53	0.95	0.89	1.07	d.l.	0.25	0.51	1.24	1.22	0.68	0.68
Dy_2O_3	3.96	3.99	4.17	3.63	5.89	0.35	3.00	3.54	5.21	5.71	4.97	5.26
Ho_2O_3	0.66	0.96	0.84	0.90	1.08	d.l.	0.84	1.01	0.86	0.92	0.98	0.98
Er_2O_3	1.80	2.70	2.13	1.97	2.82	d.l.	2.08	2.60	2.07	2.24	2.71	2.88
Tm_2O_3	0.55	0.51	0.69	0.59	0.68	0.99	0.24	0.42	0.63	0.65	0.61	0.53
Yb_2O_3	0.91	2.74	1.13	1.07	2.39	0.21	0.83	1.85	1.20	1.20	1.98	2.15
Lu_2O_3	0.36	0.65	0.39	0.38	0.75	d.l.	0.28	0.40	0.35	0.38	0.48	0.46
F	1.14	1.69	1.04	1.32	1.31	0.67	1.77	1.4	n.a.	n.a.	n.a.	n.a.
Total	85.42	89.79	84.94	91.61	90.85	87.67	89.59	83.69	93.01	92.46	92.05	90.37
P (a.p.f.u)	0.820	0.885	0.851	0.854	0.890	0.906	0.855	0.847	0.858	0.881	0.862	0.840
Si	0.084	0.054	0.065	0.085	0.067	0.029	0.055	0.058	0.070	0.051	0.098	0.101
Ti	0.008	–	–	0.005	–	–	–	0.007	–	–	–	–
Al	0.049	0.005	0.014	0.015	0.007	0.005	0.009	0.186	0.028	0.012	0.011	0.014
Mn	0.021	0.012	0.013	0.035	0.008	0.006	–	–	–	–	–	–
Fe	0.072	0.015	0.019	0.021	0.004	–	0.004	0.011	0.016	0.004	–	0.002
Ni	–	–	–	–	–	0.004	–	–	–	–	–	–
Ca	0.034	0.076	0.037	0.040	0.070	0.081	0.052	0.046	0.040	0.036	0.046	0.037
Th	–	–	–	–	–	–	–	–	–	–	–	–
Ga	–	–	–	–	–	0.016	–	–	–	–	–	–
Y	0.628	0.737	0.685	0.674	0.623	0.055	0.902	0.669	0.714	0.704	0.805	0.827
La	–	–	–	–	–	0.015	–	–	–	0.003	–	–
Ce	0.004	–	–	0.001	–	–	–	–	0.002	0.002	0.002	0.002
Pr	–	–	–	–	–	0.054	–	–	–	–	–	–
Nd	0.011	0.003	0.015	0.008	0.014	0.615	0.001	0.003	0.016	0.016	0.022	0.021
Sm	0.034	0.007	0.043	0.032	0.020	0.154	–	0.008	0.051	0.052	0.018	0.019
Eu	0.018	0.004	0.018	0.017	0.011	0.029	–	0.003	0.024	0.025	0.008	0.008
Gd	0.133	0.034	0.120	0.105	0.093	0.028	0.008	0.033	0.127	0.135	0.056	0.056
Tb	0.014	0.006	0.013	0.011	0.013	–	0.003	0.006	0.016	0.016	0.008	0.009
Dy	0.051	0.045	0.054	0.042	0.069	0.005	0.034	0.042	0.065	0.072	0.060	0.066
Ho	0.008	0.011	0.011	0.010	0.013	–	0.009	0.012	0.011	0.011	0.012	0.012
Er	0.023	0.030	0.027	0.022	0.032	–	0.023	0.030	0.025	0.028	0.032	0.035
Tm	0.007	0.006	0.009	0.007	0.008	0.014	0.003	0.005	0.008	0.008	0.007	0.006
Yb	0.011	0.029	0.014	0.012	0.027	0.003	0.009	0.021	0.014	0.014	0.023	0.025
Lu	0.004	0.007	0.005	0.004	0.008	–	0.003	0.004	0.004	0.005	0.005	0.005
F	0.144	0.188	0.133	0.151	0.152	0.094	0.194	0.162	–	–	–	–

geochemistry and mineralogy observed in the karst bauxite profiles of the Sierra de Bahoruco.

5.3. Metallurgical implications

Karst bauxite deposits from the Sierra de Bahoruco in the Dominican Republic are characterised by relatively high REE contents (up to 2.8 wt % REY in bulk) that represent a potential by-product commodity of Al. Simandl (2014), for example, reports on grades of economic interest as low as 500 ppm REO when conditions are favourable (e.g., easy open pit mining; beneficial LREE/HREE ratios; simple mineral processing). It should also be noted that not all individual REE are equal in terms of availability and necessity (a.k.a. replaceability; Du and Graedel, 2013, Nassar et al., 2015). Of special interest in the current global market are MREE (Sm-Gd) and HREE (Tb- Lu) because of their greater economic value compared with LREE (La-Nd; Gielen and Lyons, 2022). In the case of Aceitillar and El Turco karst bauxite deposits (and likely other deposits in the district) with existing economic value from high-quality Al ore (Si content ~4 wt%), the absolute contents of REE (0.12 wt% in Aceitillar and 0.76 wt% in El Turco, on average), Y (0.07 wt% in Aceitillar and 0.88 wt% in El Turco, on average), and the MREE/LREE and HREE/LREE ratios (0.22 and 0.30 in Aceitillar, and 0.89 and 1.28 in El Turco, on average, respectively) presented in this article make the case for a highly prospective ore for the extraction of REE as by-products, metallurgical considerations aside.

Since the mineralogy of REE can influence the economic potential and exploitation viability of the mining project, understanding the residence of REE in bauxite ore (carbonates, different types of

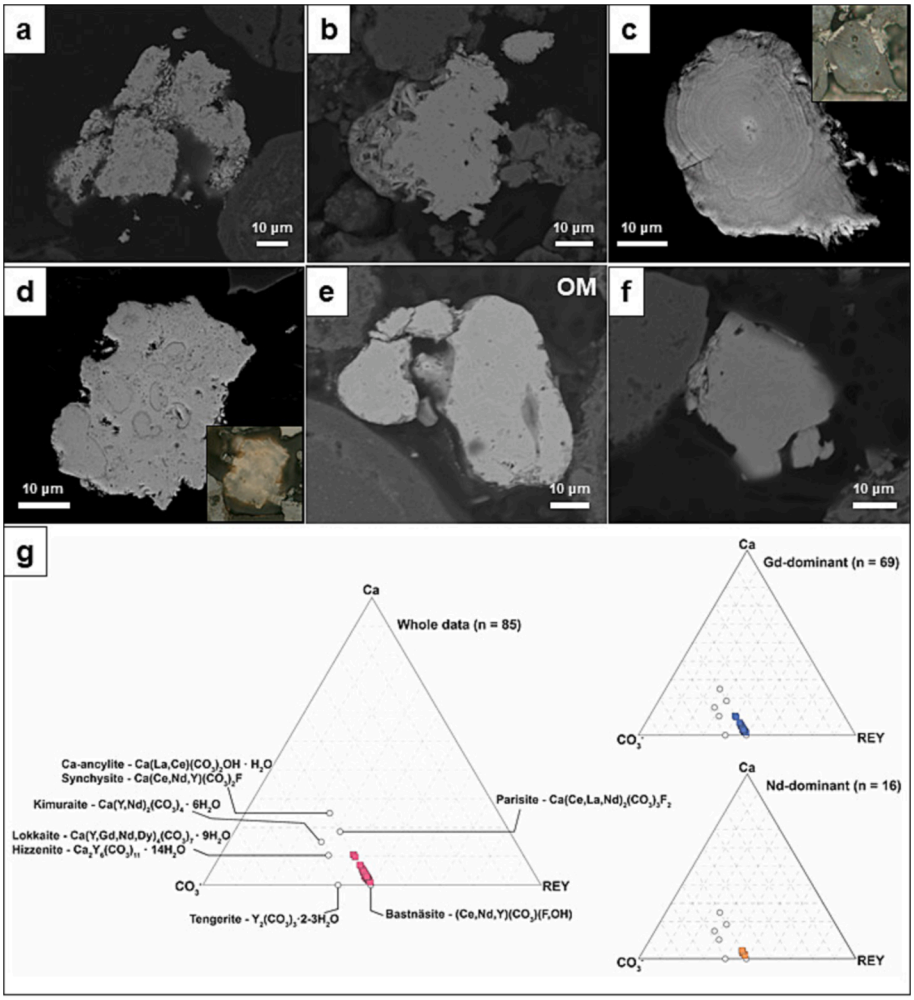

Fig. 10. BSE images (a-f) and reflected light optical micrographs (small insets in c and d) of REE-carbonate grains identified in the karst bauxites of Sierra de Bahoruco. a-d) Gd-dominant carbonates: fragmented porous aggregates (a), aggregates consisting of rod-shaped crystals (b), c) grains with concentric zoning, d) porous and internally heterogeneous grains; note the colourless appearance, low reflectivity and internal reflections in the reflected light optical micrographs in c and d. e-f) Nd-dominant carbonates: rounded (e) and subhedral (f) fragmented grains. g) Ternary diagrams showing the compositional variation of Bahoruco REE carbonates in terms of Ca and REE + Y. The ideal composition of selected REE carbonates has been included for comparison.

phosphates, oxides) is crucial for any exploration project. Therefore, an accurate mineralogical characterisation of REE minerals is important from a metallurgical point of view. During the Bayer process, REE (and other associated elements such as Sc), tend to stay unaltered in the solid phases, ending in the residue of bauxite processing (the so-called "red muds"). In fact, in red muds, LREE occur mainly as ferrotitanates and carbonates, and Y as phosphates. While the ferrotitanates are neoformed during the Bayer digestion, LREE-carbonates and Y-phosphates are resistant to the process (Agrawal and Dhawan, 2021, and references therein). Since LREE-carbonates and Y-phosphates are precisely the main mineralogy in Aceitillar and El Turco, respectively, other ore processing methods should be evaluated. The preliminary results of a pilot leaching project using bauxite samples from Greece indicate that up to 47 % of the REE in the bauxite are easily leachable using ion exchange agents like ammonium sulphate (Mouchos et al., 2016). The impact of the REE mineralogy in the bauxite ore, prior to its metallurgical processing, in the final REE contents of the respective "red muds" is yet to be evaluated.

6. Final remarks

This investigation in the deposits of Aceitillar and El Turco (SW Dominican Republic) lead to the following conclusions:

- Aceitillar and El Turco consist of mature bauxite profiles, with predominant Al oxyhydroxides and insignificant amounts of kaolinite.
- In addition to the Las Mercedes deposit, other deposits in the Pedernales Peninsula such as the ones studied in this article, contain potential REE resources.
- The REE contents in Aceitillar samples vary between 0.07 and 0.16 wt% (0.12 wt% on average), and in El Turco, between 0.28 and 1.40 wt% (0.76 wt% on average). Y ranges from 0.008 to 0.13 wt% in Aceitillar (0.07 wt% on average), and from 0.33 to 1.48 wt% in El Turco (0.88 wt% on average).
- The MREE/LREE ratio in Aceitillar is 0.22 and 0.89 in El Turco, whereas the HREE/LREE ratio is 0.30 in Aceitillar, and 1.28 in El Turco, on average.
- The REE host minerals mainly include relict monazite-(Ce), and authigenic Y-dominant phosphates, and REE carbonates, namely hydroxylbastnäsite-(Gd).
- Authigenic REE phosphates and REE carbonates appear concentrated in different bauxite profiles, suggesting particular controls in their environment of deposition during the bauxitisation process.
- The predominance diagrams obtained are consistent with the REE mineralogy in Aceitillar and El Turco (carbonates versus phosphates) and the coexisting minerals (gibbsite, Mn oxyhydroxides). The conditions at El Turco would indicate more oxic and acidic than in Aceitillar.
- Further data is needed to precisely identify some of the REE-bearing minerals, and the presence of new mineral species (e.g., Gd-dominant carbonates) is possible.

Table 5
Representative EMP analyses of REE-carbonates from the Sierra de Bahoruco bauxite deposits (n.a.: not analysed; d.l.: below detection limit). FeOt: total Fe, OH and CO_3 are calculated according to Table 1.

Label	528	533	549	566	572	576	583	590	601	897	926	949
Deposit	**Aceitillar**											
SiO_2 (wt.%)	1.17	0.40	d.l.	0.92	0.38	0.57	0.57	d.l.	1.31	n.a.	n.a.	n.a.
TiO_2	d.l.	d.l.	d.l.	d.l.	d.l.	d.l.	d.l.	d.l.	d.l.	n.a.	n.a.	n.a.
Al_2O_3	d.l.	d.l.	d.l.	0.10	d.l.	0.40	d.l.	d.l.	d.l.	d.l.	0.80	d.l.
MnO	d.l.	d.l.	d.l.	d.l.	d.l.	d.l.	0.13	d.l.	d.l.	0.30	d.l.	d.l.
FeOt	d.l.	d.l.	d.l.	d.l.	d.l.	d.l.	d.l.	d.l.	d.l.	d.l.	0.69	d.l.
CoO	d.l.	d.l.	d.l.	d.l.	n.a.	n.a.	n.a.	d.l.	d.l.	n.a.	n.a.	n.a.
NiO	d.l.	d.l.	d.l.	d.l.	d.l.	0.11	0.06	d.l.	d.l.	n.a.	n.a.	n.a.
CaO	1.01	2.19	0.66	0.98	1.05	1.31	0.64	1.86	1.67	1.08	0.71	1.82
BaO	n.a.	n.a.	n.a.	n.a.	n.a.	n.a.	n.a.	n.a.	n.a.	d.l.	d.l.	d.l.
SrO	n.a.	n.a.	n.a.	n.a.	n.a.	n.a.	n.a.	n.a.	n.a.	d.l.	d.l.	d.l.
UO_2	n.a.	n.a.	n.a.	n.a.	n.a.	n.a.	n.a.	n.a.	n.a.	0.27	d.l.	d.l.
ThO_2	n.a.	n.a.	n.a.	n.a.	n.a.	n.a.	n.a.	n.a.	n.a.	d.l.	d.l.	d.l.
Ga_2O_3	0.82	0.21	0.59	0.25	0.28	0.91	0.43	0.06	0.10	n.a.	n.a.	n.a.
Y_2O_3	1.92	2.60	1.89	1.69	3.33	1.61	0.64	2.06	3.06	0.84	2.92	6.48
La_2O_3	0.93	2.48	0.97	1.19	0.55	1.83	5.96	2.26	0.45	0.46	d.l.	d.l.
Ce_2O_3	d.l.	d.l.	d.l.	d.l.	d.l.	d.l.	d.l.	d.l.	d.l.	d.l.	d.l.	d.l.
Pr_2O_3	0.74	0.94	0.74	1.07	0.16	1.60	4.84	1.92	d.l.	2.15	0.23	d.l.
Nd_2O_3	12.26	15.54	12.79	13.98	4.67	19.86	40.11	23.57	4.37	28.59	6.99	5.30
Sm_2O_3	14.29	8.74	13.95	14.79	6.73	15.42	7.15	11.68	5.85	18.60	8.16	6.52
Eu_2O_3	5.12	3.60	4.87	5.01	3.46	4.92	2.36	3.38	3.17	4.74	3.46	3.25
Gd_2O_3	25.76	23.45	26.93	24.86	38.03	17.47	4.77	16.06	38.39	8.45	34.19	32.66
Tb_2O_3	1.55	1.52	1.86	1.45	3.47	0.76	d.l.	0.72	3.57	0.53	3.54	3.24
Dy_2O_3	1.12	3.28	1.69	1.04	4.39	0.40	0.33	2.11	4.52	0.75	6.54	6.77
Ho_2O_3	d.l.	0.34	d.l.	d.l.	0.15	d.l.	d.l.	0.13	0.14	d.l.	d.l.	0.27
Er_2O_3	0.13	0.34	0.08	0.18	0.42	d.l.	d.l.	0.21	0.47	d.l.	0.27	0.47
Tm_2O_3	1.54	1.09	1.50	1.55	0.90	1.66	0.75	1.33	0.91	0.80	d.l.	d.l.
Yb_2O_3	0.20	0.13	d.l.	d.l.	d.l.	0.12	d.l.	0.18	d.l.	0.17	d.l.	0.16
Lu_2O_3	d.l.	0.23	0.08	d.l.	0.31	d.l.	d.l.	0.12	0.37	0.15	0.37	0.38
P_2O_5	d.l.	d.l.	d.l.	d.l.	0.19	d.l.	d.l.	d.l.	d.l.	d.l.	d.l.	d.l.
F	d.l.	d.l.	d.l.	d.l.	d.l.	d.l.	d.l.	d.l.	d.l.	d.l.	d.l.	d.l.
CO3 (calc)	24.26	24.88	24.32	24.30	24.19	24.88	24.75	25.08	24.21	24.33	23.66	25.09
OH (calc)	6.87	7.05	6.89	6.89	6.86	7.05	7.01	7.11	6.86	6.90	6.71	7.11
Total	99.69	99.02	99.81	100.25	99.52	100.98	100.55	99.85	99.41	99.11	99.25	99.52
Si	0.048	0.016	–	0.038	0.016	0.023	0.023	–	0.054	–	–	–
Ti	–	–	–	–	–	–	–	–	–	–	–	–
Al	–	–	–	0.005	–	0.019	–	–	–	–	0.040	–
Mn	–	–	–	–	–	–	0.004	–	–	0.010	–	–
Fe	–	–	–	–	–	–	–	–	–	–	0.020	–
Co	–	–	–	–		–	–	–	–	–	–	–
Ni	–	–	–	–	–	0.003	0.002	–	–	–	–	–
Ca	0.045	0.094	0.029	0.043	0.046	0.056	0.028	0.079	0.074	0.048	0.032	0.078
Ba	–	–	–	–	–	–	–	–	–	–	–	–
Sr	–	–	–	–	–	–	–	–	–	–	–	–
U	–	–	–	–	–	–	–	–	–	0.020	–	–
Th	–	–	–	–	–	–	–	–	–	–	–	–
Ga	0.022	0.006	0.016	0.007	0.007	0.023	0.011	0.002	0.003	–	–	–
Y	0.042	0.056	0.041	0.037	0.073	0.034	0.014	0.044	0.067	0.018	0.066	0.137284622
La	0.014	0.037	0.015	0.018	0.008	0.027	0.089	0.033	0.007	0.007	–	–
Ce	–	–	–	–	–	–	–	–	–	–	–	–
Pr	0.011	0.014	0.011	0.016	0.002	0.023	0.071	0.028	–	0.032	0.004	–
Nd	0.180	0.223	0.188	0.205	0.069	0.285	0.578	0.335	0.064	0.419	0.105	0.075
Sm	0.203	0.121	0.197	0.209	0.096	0.213	0.099	0.160	0.083	0.263	0.119	0.089
Eu	0.072	0.049	0.068	0.070	0.049	0.067	0.033	0.046	0.045	0.066	0.050	0.044
Gd	0.352	0.312	0.367	0.339	0.520	0.233	0.064	0.212	0.525	0.115	0.478	0.431
Tb	0.021	0.020	0.025	0.020	0.047	0.010	–	0.009	0.048	0.007	0.049	0.042
Dy	0.015	0.042	0.022	0.014	0.058	0.005	0.004	0.027	0.060	0.010	0.089	0.087
Ho	–	0.004	–	–	0.002	–	–	0.002	0.002	–	–	0.003
Er	0.002	0.004	0.001	0.002	0.005	–	–	0.003	0.006	–	0.004	0.006
Tm	0.020	0.014	0.019	0.020	0.012	0.021	0.009	0.016	0.012	0.010	–	–
Yb	0.002	0.002	–	–	–	0.002	–	0.002	–	0.002	–	0.002
Lu	–	0.003	0.001	–	0.004	–	–	0.001	0.005	0.002	0.005	0.005
P	–	–	–	–	0.006	–	–	–	–	–	–	–
F	–	–	–	–	–	–	–	–	–	–	–	–
CO_3	1	1	1	1	1	1	1	1	1	1	1	1
OH	1	1	1	1	1	1	1	1	1	1	1	1

Declaration of Competing Interest

The authors declare that they have no known competing financial interests or personal relationships that could have appeared to influence the work reported in this paper.

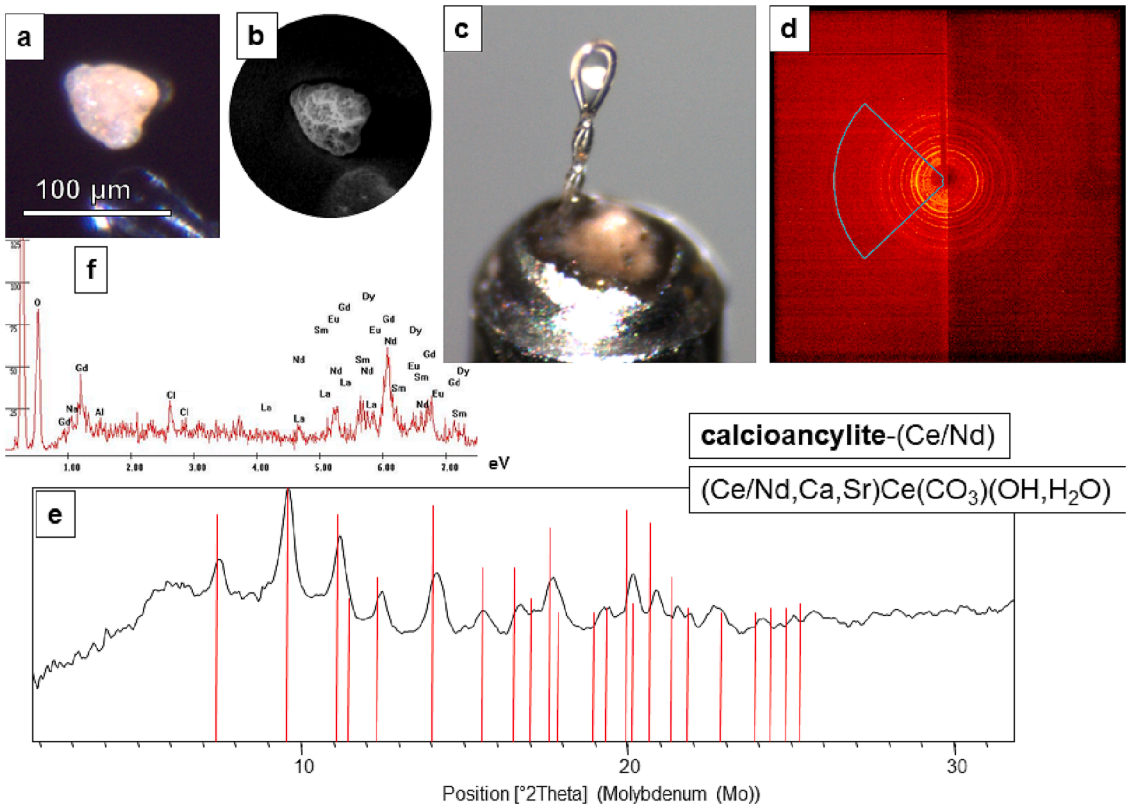

Fig. 11. Image of the handpicked REE carbonate grain selected for monocrystal XRD (a: binocular; b: secondary electron SEM; c: binocular, when inserted in the sample holder). The results (d: raw data; e: processed X-ray diffractogram) indicate that the mineral has a calcioancylite structure, and the SEM-EDS shows that it is enriched in Gd, Nd, Sm and Eu (f).

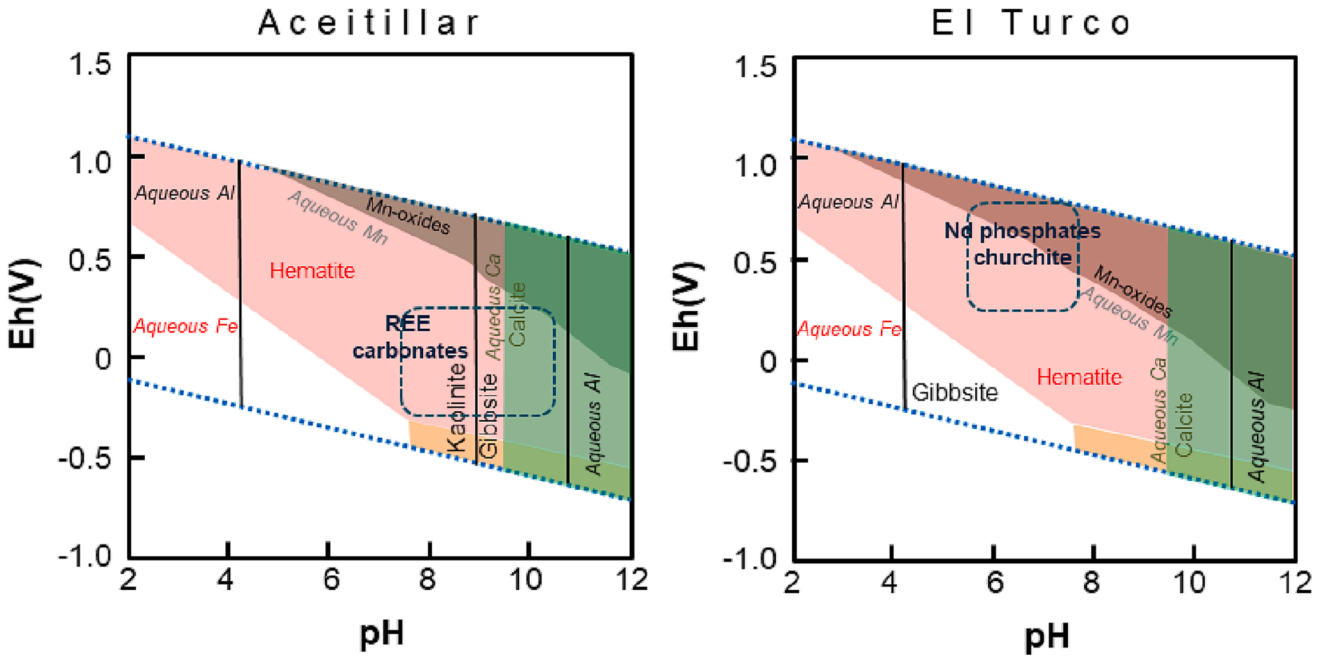

Fig. 12. Stability diagrams for the deposits of Aceitillar (left) and El Turco (right), performed with PhreePlot®.

Data availability

Data will be made available on request.

Acknowledgements

This research has been funded by the MESCYT (Ministry of Higher Education, Science and Technology of the Dominican Republic) projects 2014-1B4-133 and 2022-1A4-189. Additional funding has been

provided by the Spanish project PID2019-105625RB-C21 (IP J.A. Proenza). This paper has been produced within the framework of the MinResET (Mineral Resources for the Energy Transition) research group (2021-SGR-00239, Agència de Gestió d'Ajuts Universitaris i de Recerca de Catalunya). We are grateful to Bernhard Dold, Edwin García, Ramón Elías Ramírez and Santiago Muñoz for their collaboration and support, to DOVEMCO for their hospitality, and to driver Wilson and Miguel, and assistants Johny and Lily for their inestimable help, during the field work campaigns. Sincere thanks are also extended to the two Reviewers for their kind remarks, and their thorough and constructive suggestions that helped to improve the quality of the manuscript.

References

Agrawal, S., Dhawan, N., 2021. Evaluation of red mud as a polymetallic source – A review. Miner. Eng. 171, 107084.

Aiglsperger, T., Dold, B., Proenza, J.A., Villanova-de-Benavent, C., 2019. Geochemistry of REE-rich karst bauxite ore deposits from the Sierra de Bahoruco, Dominican Republic. In: Proceedings of the 15th SGA Biennial Meeting, 27-30 August, University of Glasgow Publicity Services, Vol. 4, 1834-1836.

Aiglsperger, T., Proenza, J.A., Zaccarini, F., Lewis, J.F., Garuti, G., Labrador, M., Longo, F., 2015. Platinum group minerals (PGM) in the Falcondo Ni laterite deposit, Loma Caribe peridotite (Dominican Republic). Miner. Deposita 50, 105–123.

Bárdossy, G., 1982. Karst bauxites. Bauxite deposits on carbonate rocks. Developments in Economic Geology, 1st ed., Elsevier: Budapest, Hungary, volume 14, pp. 441.

Boynton, W.V., 1984. Geochemistry of rare earth elements: meteorite studies. In: Henderson, P. (Ed.), Rare Earth Element Geochemistry. Elsevier, New York, pp. 63–114.

Bray, E.L., 2017. Aluminum. USGS Mineral Commodity Summaries 22–24.

Chakhmouradian, A.R., Wall, F., 2012. Rare earth elements: minerals, mines, magnets (and more). Elements 8, 333–340.

Commission, E., 2020. Study on the EU's list of Critical Raw Materials (Final Report). European Commission, Brussels, pp. 1–158.

Cordier, D.J., 2021. USGS Mineral Commodity Summaries: Rare Earths. Available at: https://pubs.usgs.gov/periodicals/mcs2022/mcs2022-rare-earths.pdf.

de León, O., 1989. Geología de la Sierra de Bahoruco (República Dominicana). Museo Nacional de Historia Natural: Santo Domingo, Dominican Republic, 112 p.

Deady, E., Mouchos, E., Goodenough, K., Williamson, B., Wall, F., 2014. Rare Earth Elements in karst-bauxites: A novel untapped European resource? ERES 2014: 1st conference on European Rare Earth Resources (Milos, Greece), 364-375.

Du, X., Graedel, T.E., 2013. Uncovering the end uses of the rare earth elements. Sci. Total Environ. 461–462, 781–784.

Dutta, T., Kim, K.H., Uchimiya, M., Kwon, E.E., Jeon, B.H., Deep, A., Yun, S.T., 2016. Global demand for rare earth resources and strategies for green demand. Environ. Res. 150, 182–190.

Escuder-Viruete, J., Joubert, M., Abad, M., Pérez-Valera, F., Gabites, J., 2016. The basaltic volcanism of the Dumisseau Formation in the Sierra de Bahoruco, SW Dominican Republic: A record of the mantle plume-related magmatism of the Caribbean Large Igneous Province. Lithos 254–255, 67–83.

Gamaletsos, P., Godelitsas, A., Mertzimekis, T.J., Göttlicher, J., Steininger, R., Xantos, S., Berndt, J., Klemme, S., Kuzmin, A., Bárdossy, G., 2011. Thorium partitioning in Greek industrial bauxite investigated by synchrotron radiation and laser-ablation techniques. Nucl. Instrum. Methods Phys. Res., Sect. B 269, 3067–3073.

Gamboji, J., 2017. Rare earth elements. USGS Mineral Commodity Summaries 134–135.

Gielen, D., Lyons, M., 2022. Critical Materials for the Energy Transition: Rare Earth Elements. International Renewable Energy Agency, Abu Dhabi. Available at: https://www.irena.org/-/media/Files/IRENA/Agency/Technical-PapersIRENA_Rare_Earth_Elements_2022.pdf.

Goldich, S.S., Bergquist, H.R., 1947. Aluminous lateritic soils of the Sierra de Bahoruco Area Dominican Republic, W.I. Geologic Investigations in the American Republics. United States Government Printing Office Washington, p. 53-84.

Goodenough, K.M., Wall, F., Merriman, D., 2017. The Rare Earth Elements: demand, global resources, and challenges for resourcing future generations. Nat. Resour. Res. 27, 201–216. https://doi.org/10.1007/s11053-017-9336-5.

Gu, J., Huang, Z., Fan, H., Jin, Z., Yan, Z., Zhang, J., 2013. Mineralogy, geochemistry, and genesis of lateritic bauxite deposits in the Wuchuan–Zheng'an–Daozhen area, Northern Guizhou Province, China. J. Geochem. Explor. 130, 44–59. https://doi.org/10.1016/j.gexplo.2013.03.003.

International Energy Agency-IEA (2021). The Role of Critical Minerals in Clean Energy Transitions. World Energy Outlook Special Report (available at www.iea.org).

Kalatha, S., Perraki, M., Economou-Eliopoulos, M., Mitsis, I., 2017. On the Origin of Bastnaesite-(La, Nd, Y) in the Nissi (Patitira) Bauxite Laterite Deposit, Lokris, Greece. Minerals 7 (3), 45.

Kinniburg, D.G., Cooper, D.M., 2011. Creating graphical output with PHREEQC, available online: http://www.phreeplot.org.

Laskou, M., Andreou, G., 2003. Rare earth elements distribution and REE-minerals from the Parnassos-Ghiona bauxite deposits, Greece. In: Eliopoulos, D. (Ed.), Mineral Exploration and Sustainable Development, 7th Biennial SGA Meeting, Athens. Mill Press, Rotterdam.

Lewis, J.F., Draper, G., 1991. Geology and tectonic evolution of the Northern Caribbean margin. In The Geology of North America H: The Caribbean region. In: Dengo, G., Case, J.E., Geological Society of America: Boulder, Colorado, United States of America, volume H, 77-140.

Li, Z., Din, J., Xu, J., Liao, C., Yin, F., Tao, L., Cheng, L., Li, J., 2013. Discovery of the REE minerals in the Wulong-Nanchuan bauxite deposits Chongqing, China: Insights on conditions of formation and processes. J. Geochem. Explor. 133, 88–102.

Lidiak, E.G., Anderson, T.H., 2015. Evolution of the Caribbean plate and origin of the Gulf of Mexico in light of plate motions accommodated by strike-slip faulting. In: Late Jurassic Margin of Laurasia-A Record of Faulting Accommodating Plate Rotation, Anderson, T.H., Didenko, A.N., Johnson, C.L., Khanchuk, A.I., MacDonald, J.H., Jr., Geological Society of America Special Paper: Boulder, Colorado, United States of America 513, SPE513–01.

Liu, X., Wang, Q., Zhang, Q., Zhang, Y., Li, Y., 2016. Genesis of REE minerals in the karstic bauxite in western Guangxi, China, and its constraints on the deposit formation conditions. Ore Geol. Rev. 75, 100–115.

Lymperopoulou, T.H., 1996. Determination and Recovery of Rare Earth Elements from Bauxites and Red Mud [PhD thesis]. National Technical University of Athens (in Greek).

Maksimović, Z., Pantó, G., 1991. Contribution to the geochemistry of the rare earth elements in the karst-bauxite deposits of Yugoslavia and Greece. Geoderma 51, 93–109.

Maksimović, Z., Pantó, G., 1996. Authigenic rare earth minerals in karst-bauxites and karstic nickel deposits. In: Jones, A.P., Wall, F., Williams, C.T. (Eds.), Rare Earth Minerals: Chemistry, Origin and Ore Deposits, 10;. Chapman & Hall, London, pp. 257–279.

Mameli, P., Mongelli, G., Oggiano, G., Dinelli, E., 2007. Geological, geochemical and mineralogical features of some bauxite deposits from Nurra (Western Sardinia, Italy): insights on conditions of formation and parental affinity. Int. J. Earth Sci. 96, 887–902.

Mann, P., 2007. Overview of the tectonic history of northern Central America. Geological Society of America Special Papers 428, 1-19, 10.1130/2007.2428(01).

Mondillo, N., Balassone, G., Boni, M., Rollinson, G., 2011. Karst bauxites in the Campania Apennines (southern Italy): A new approach. Period. Mineral. 80 (3), 407–432.

Mondillo, N., Balassone, G., Boni, M., Chelle-Michou, C., Cretella, S., Mormone, A., Putzolu, F., Santoro, L., Scognamiglio, G., Tarallo, M., 2019. Rare earth elements (REE) in Al- and Fe-(Oxy)-hydroxides in bauxites of Provence and Languedoc (Southern France): implications for the potential recovery of REEs as by-products of bauxite mining. Minerals 9, 504.

Mongelli, G., 1997. Ce-anomalies in the textural components of Upper Cretaceous karst bauxites from the Apulian carbonate platform (southern Italy). Chem. Geol. 140, 69–79.

Mouchos, E., Wall, F., Williamson, B.J., Palumbo-Roe, B., 2016. Easily leachable rare earth element phases in the Parnassus-Giona bauxite deposits, Greece. Bull. Geol. Soc. Greece 50, 1952–1958.

Nassar, N.T., Du, X., Graedel, T.E., 2015. Criticality of the rare earth elements. J. Ind. Ecol. 19, 1044–1054.

Ochsenkühn-Petropulu, M., Ochsenkühn, K.M., 1995. Rare earth minerals found in Greek bauxites by scanning electron microscopy and electron probe micro-analysis. Eur. Microsc. Anal. 37, 33–34.

Pantó, G., Maksimović, Z., 2001. Two new rare earth minerals in an unusual mineralization of the Nissi bauxite deposit, Greece. Acta Geol. Hung. 44 (1), 81–93.

Parkhurst, D.L., Appelo, C.A.J., 2013. Description of input and examples for PHREEQC version 3—A computer program for speciation, batch-reaction, one-dimensional transport, and inverse geochemical calculations. Available online: US Geol. Surv. Tech. Methods 6, 497 https://pubs.usgs.gov/tm/06/a43/pdf/tm6-A43.pdf.

Pérez-Valera, F., Abad, M., 2010. Informe Estratigráfico y Sedimentológico. Proyecto 1B de la Cartografía Geotemática de la República Dominicana. Programa SYSMIN. Dirección General de Minería, Santo Domingo, Dominican Republic.

Pérez-Valera, F., 2010. Geologic Map Sheet 1:50.000 num. 5970-III and corresponding memoir. Proyecto 1B de Cartografía Geotemática de la República Dominicana. Programa SYSMIN. Dirección General de Minería, Santo Domingo, Dominican Republic.

Proenza, J.A., Aiglsperger, T., Villanova-de-Benavent, C., Torró, L., Rodríguez, D., Ramírez, A., Rodríguez, J., 2017. Discovery of REE minerals hosted in karst bauxite ores from the Sierra de Bahoruco, Pedernales, Dominican Republic. In Proceedings of the 14th SGA Biennial Meeting, Québec City, QC, Canada, 20–23 August 2017, Volume 4, p. 5.

Proenza, J.A., Villanova-de-Benavent, C., Torró, L., Aiglsperger, T., Ramírez, A., Rodríguez, J., 2021. Recursos de tierras raras en la Rep. Dominicana: Bauxitas kársticas de la Sierra de Bahoruco. Geo-Noticias 17 (46), 21–25. ISSN: 2636-1891.

Putzolu, F., Piccolo Papa, A., Mondillo, N., Boni, M., Balassone, G., Mormone, A., 2018. Geochemical Characterization of Bauxite Deposits from the Abruzzi Mining District (Italy). Minerals 8, 298.

Radusinović, S., Papadopoulos, A., 2021. The Potential for REE and Associated Critical Metals in Karstic Bauxites and Bauxite Residue of Montenegro. Minerals 11, 975.

Ramírez, R.E., 2015. El oro de Pedernales. Geonoticias 38 (12), 12–14.

Reinhardt, N., Proenza, J., Villanova-de-Benavent, C., Aiglsperger, T., Bover-Arnal, T., Torró, L., et al., 2018. Geochemistry and Mineralogy of Rare Earth Elements (REE) in Bauxitic Ores of the Catalan Coastal Range, NE Spain. Minerals 8, 562.

Rudashevsky, N.S., Rudashevsky, V.N., 2007. Patent of Russian Federation #69418, industrial (useful) model, "Device for separation of solid particles", Moscow, December 27.

Simandl, G.J., 2014. Geology and market-dependent significance of rare earth element resources. Mineral. Deposita 49, 889–904.

Smith Stegen, K., 2015. Heavy rare earths, permanent magnets, and renewable energies: An imminent crisis. Energy Policy 79, 1–8.

Spahiu, K., Bruno, J. A., 1995. Selected thermodynamic database for REE to be used in hlnw performance assessment exercises, SKB Technical Report TR 95-35, 80 p.

Torró, L., Proenza, J.A., Aiglsperger, T., Bover-Arnal, T., Villanova-de-Benavent, C., Rodríguez-García, D., Ramírez, A., Rodríguez, J., Mosquea, L.A., Salas, R., 2017. Geological, geochemical and mineralogical characteristics of REE-bearing Las Mercedes bauxite deposit, Dominican Republic. Ore Geol. Rev. 89, 114–131.

Villanova-de-Benavent, C., Proenza, J.A., Aiglsperger, T., Torró, L., Domènech, C., Rodríguez, J., Ramírez, A., Dold, B., 2021. REE enrichment in the karst bauxites of Pedernales/Sierra de Bahoruco (Dominican Republic). Goldschmidt abstracts.

Villanova-de-Benavent, C., Proenza, J.A., Torró, L., Aiglsperger, T., García-Casco, A., Altamirano-Morán, D., Ramirez, A., Rodríguez, J., 2017. Secondary REE-Minerals in the Karst Bauxites of the Bahoruco Peninsula (Dominican República). Macla 22, 125–126.

Villanova-de-Benavent, C., Proenza, J.A., Aiglsperger, T., Torró, L., Domènech, C., Domínguez-Carretero, D., Ramírez, A., Rodríguez, J., 2022. REE en las bauxitas kársticas de la Sierra de Bahoruco (República Dominicana): geoquímica y mineralogía. Macla 26, 196–197.

Vind, J., Malfliet, A., Blanpain, B., Tsakiridis, P.E., Tkaczyk, A.H., Vassiliadou, V., Panias, D., 2018. Rare earth element phases in bauxite residue. Minerals 8, 77.

Wall, F., 2014. Rare earth elements. In: Gunn, G. (Ed.), Critical Metals Handbook, 1st. American Geophysical Union, United States of America, pp. 312–339.

Wang, Q., Deng, J., Liu, X., Zhang, Q., Sun, S., Jiang, C., Zhou, F., 2010. Discovery of the REE minerals and its geological significance in the Quyang bauxite deposit, West Guangxi, China. J. Asian Earth Sci. 39, 701–712.

Weng, Z., Jowitt, S.M., Mudd, G.M., Haque, N., 2015. A detailed assessment of global rare earth element resources: Opportunities and challenges. Econ. Geol. 110 (8), 1925–1952.

Yang, S., Wang, Q., Deng, J., Wang, Y., Kang, W., Liu, X., Li, Z., 2019. Genesis of karst bauxite-bearing sequences in Baofeng, Henan (China), and the distribution of critical metals. Ore Geol. Rev. 115, 103161.

Zeug, M., Nasdala, L., Ende, M., Habler, G., Hauzenberger, C., Chanmuang N, C., Škoda, R., Topa, D., Wildner, M, Wirth, R., 2021. The parisite–(Ce) enigma: challenges in the identification of fluorcarbonate minerals. Mineralogy and Petrology, 115, 1–19.